Master's Thesis

Study on Functional Devices Using Ultrathin Metal Nanostrips

Jungsan Kim

Department of Electrical Engineering

Graduate School of UNIST

2019

Study on Functional Devices Using Ultrathin Metal Nanostrips

Jungsan Kim

Department of Electrical Engineering

Graduate School of UNIST

Study on Functional Devices Using Ultrathin Metal Nanostrips

A thesis
submitted to the Graduate School of UNIST
in partial fulfillment of the
requirements for the degree of
Master of Science

Jungsan Kim

12/14/2018 of submission

Approved by

Advisor
Min-Suk Kwon

Study on Functional Devices Using Ultrathin Metal Nanostrips

Jungsan Kim

This certifies that the thesis of Jungsan Kim is approved.

12/14/2018 of submission

signature

Advisor: Min-Suk Kwon

signature

Jongwon Lee: Thesis Committee Member #1

signature

Jiwon Chang: Thesis Committee Member #2

Abstract

Infrared (IR) wireless communications has been widely studied due to advantages such as a large bandwidth and immunity to electromagnetic interference. Directly modulated light emitting diodes (LEDs) are usually used as a light source. In this case, however, the nature of LEDs limits modulation speed. In this thesis, an external modulator based on an ultrathin silver (Ag) film and an Ag strip array is theoretically investigated to solve the modulation speed limit problem. The investigated modulator consists of an ultrathin Ag film, a hafnium oxide (HfO_2) layer, and a periodic array of a stack of an indium-tin-oxide (ITO) strip and an ultrathin Ag strip. 850 nm free-space beam incident on the array generates localized surface plasmon resonance (LSPR) around the Ag strip. The LSPR results in a rejection band in the transmission spectrum of the modulator. The Ag film, the HfO_2 layer, and the ITO strip comprise a sort of metal-oxide-semiconductor (MOS) structure. By using the MOS structure, the optical properties of the ITO strip are electrically controlled, and the LSPR is tuned in consequence. In this way, the transmission of the modulator is modulated at a wavelength of 850 nm. The optical characteristics of the modulator are analyzed with respect to its geometrical parameters by using the finite difference time domain (FDTD) method. For the analysis, the optical properties of the ITO strip are obtained by analyzing electrically the MOS structure and using the Drude model. When a bias voltage of 46 V is applied between the Ag film and the Ag strip, the transmission at a wavelength of 850 nm is increased by 200 %. A preliminary experiment for realization of the modulator is carried out. E-beam lithography and lift-off processes are established. By using the processes, subtractive color filters based on an array of thin gold strips are fabricated and characterized. The experimental results show good agreement with the simulation results. The processes will be used to realize the modulator.

Contents

List of Figures

Figure 2-8. Influence of the oxide thickness t_H of the proposed modulator.

Figure 2-9. The E_y field of the two resonance dips when w = 97 nm, p = 291 nm (3w), t_M = 10 nm, t_H = 10 nm, and θ = 0°. (a) The E_y field distribution at λ_r = 726 nm and (b) the E_y field distribution at λ_r = 866 nm.

Figure 2-10. Influence of the incident angle of the proposed modulator.

Figure 2-11. The electric field distribution of the proposed modulator in DEVICE simulation (Lumerical Inc.). The yellow dashed line is the edge of the HfO_2, and the Ag strip and the Ag layer are not indicated in the figure.

Figure 2-12. The carrier concentration distribution of the ITO strip when there is a bias voltage between the Ag strip and the Ag layer. The interface between HfO_2 and ITO is at y = 0. The carrier concentration is indicated in black solid line (0 V bias) and red solid line (46 V bias).

Figure 2-13. The change of the ITO strip refractive index according to the change of the carrier concentration in the ITO strip. The red region HfO_2 and the blue region is ITO. The Re[N_{ITO}] is indicated in solid lines and the Im[N_{ITO}] is indicated in dashed lines.

Figure 2-14. The transmission spectrum when there is a bias voltage between the Ag strip and the Ag layer. The black solid line is when the bias voltage V = 0 V, and the red solid line is when the bias voltage V = 46 V.

Figure 2-15. The transmission spectrum when there is a bias voltage between the Ag strip and the Ag layer. (a) the intensity modulation when w = 148 nm, p = 444 nm (3w), t_M = 10 nm, t_H = 10 nm, and θ = 0°, and (b) the intensity modulation when w = 93 nm, p = 279 nm (3w), t_M = 10 nm, t_H = 10 nm, and θ = 0°

Figure 3-1. Fabrication process of the unit cell of simple metal strip array.

Figure 3-2. SEM image of the fabricated pattern with w = 50 nm and p = 150 nm.

Figure 3-3. SEM image of fabricated color filters. (a), (b), and (c) are w = 100 nm with p = 300 nm, w = 90 nm with p = 300 nm, and w = 80 nm with p = 300 nm, respectively. (d), (e), and (f) are magnified

image of (a), (b), and (c), respectively.

Figure 3-4. (a) The image of the UV-Vis microspectrometer and (b) schematic of experimental setup.

Figure 3-5. (a) The transmission image and (b) the reflection image of the patterns from the UV-Vis microspectrometer.

Figure 3-6. The transmission spectrum of simulation and measurement results. Black solid line indicates the result of the simulation, and red, blue, and pink solid lines indicate the measurement results of the patterns when w = 100 nm and p = 300 nm, w = 90 nm and p = 300 nm, and w = 80 nm and p = 300 nm, respectively.

Nomenclature

SPPs	Surface plasmon polaritons
TM	Transverse magnetic
TE	Transverse electric
IMI	Insulator-metal-insulator
LRSPP	Long-range surface plasmon polariton
SRSPP	Short-range surface plasmon polariton
FDTD	Finite difference time domain
FP	Fabry-Perot
LSPR	Localized surface plasmon resonance
IR	Infrared
Li-Fi	Light fidelity
LEDs	Light emitting diodes
VCSELs	Vertical cavity surface emitting lasers
ITO	Indium-tin-oxide
TCOs	Transparent conducting oxides
MOS	Metal-oxide-semiconductor

ER	E-beam resist

I. Introduction

1.1. Surface plasmon polaritons at a metal film

Surface plasmon polaritons (SPPs) are electromagnetic excitations propagating at the interface between a dielectric and a conductor, evanescently confined in the perpendicular direction. These electromagnetic surface waves via the coupling of the electromagnetic fields to oscillations of the conductor's electron plasma [1]. The interaction between a conductor and an electromagnetic wave can be understood as the Maxwell's equations.

We thus take as a starting point the Maxwell's equations of macroscopic electromagnetism in the following form:

$$\nabla \cdot \mathbf{D} = \rho_{ext} \tag{1.1}$$

$$\nabla \cdot \mathbf{B} = 0 \tag{1.2}$$

$$\nabla \times \mathbf{E} = -\frac{\partial \mathbf{B}}{\partial t} \tag{1.3}$$

$$\nabla \times \mathbf{H} = \mathbf{J}_{ext} + \frac{\partial \mathbf{D}}{\partial t} \tag{1.4}$$

where, **D** is the dielectric displacement, **E** is the electric field, **H** is the magnetic field, **B** is the magnetic induction or magnetic flux density, ρ_{ext} is the external charge, and $\mathbf{J}_{ext}$ is the current density.

The four macroscopic fields are linked via the polarization **P** and magnetization **M** by

$$\mathbf{D} = \varepsilon_0 \mathbf{E} + \mathbf{P} \tag{1.5}$$

$$\mathbf{H} = \frac{1}{\mu_0}\mathbf{B} - \mathbf{M} \tag{1.6}$$

where, ε_0 is the electric permittivity and μ_0 is the magnetic permeability of vacuum. In this thesis, since only nonmagnetic media is treated, magnetization **M** need not be considered. **P** describes the electric dipole moment per unit volume inside the material. It is related to the internal charge density

via $\nabla \cdot \mathbf{P} = -\rho$. Charge conservation ($\nabla \cdot \mathbf{J} = -\partial\rho/\partial t$) requires that the internal charge and current densities are linked via

$$\mathbf{J} = \frac{\partial \mathbf{P}}{\partial t} \tag{1.7}$$

The great advantage of this approach is that the macroscopic electric field includes all polarization effects.

$$\nabla \cdot \mathbf{E} = \frac{\rho_{tot}}{\varepsilon_0} \tag{1.8}$$

In linear, isotropic and nonmagnetic media, the constitutive relations are,

$$\mathbf{D} = \varepsilon_0 \varepsilon \mathbf{E} \tag{1.9}$$

$$\mathbf{B} = \mu_0 \mu \mathbf{H} \tag{1.10}$$

where, ε is the dielectric constant or relative permittivity and $\mu = 1$ represents the relative permeability of the nonmagnetic medium. The linear relationship between **D** and **E** is often also implicitly defined using the dielectric susceptibility χ, which describes the linear relationship between **P** and **E** via

$$\mathbf{P} = \varepsilon_0 \chi \mathbf{E} \tag{1.11}$$

The last important constitutive linear relationship is that between the internal current density **J** and the electric field **E**, defined via the conductivity σ by

$$\mathbf{J} = \sigma \mathbf{E} \tag{1.12}$$

In order to investigate the physical properties of SPPs, the equations in a general form applicable to the guiding of electromagnetic waves, the wave equation, is required. In the absence of external charge and current densities, the curl equations (1.3, 1.4) can be combined to yield

$$\nabla \times \nabla \times \mathbf{E} = -\mu_0 \frac{\partial^2 \mathbf{D}}{\partial t^2} \tag{1.13}$$

Using the vector identities with the assumption that negligible variation of the dielectric profile $\varepsilon = \varepsilon(\mathbf{r})$ over distances on the order of one optical wavelength, the equation can be simplified to the central equation of electromagnetic theory,

$$\nabla^2 \mathbf{E} - \frac{\varepsilon}{c^2} \frac{\partial^2 \mathbf{E}}{\partial t^2} = 0 \tag{1.14}$$

By assuming that in all generality a harmonic time dependence $\mathbf{E}(\mathbf{r}, \mathrm{t}) = \mathbf{E}(\mathbf{r}) e^{-i\omega t}$ of the electric field, the equation (1.14) becomes,

$$\nabla^2 \mathbf{E} + \mathrm{k}_0^2 \varepsilon \mathbf{E} = 0 \tag{1.15}$$

where $\mathrm{k}_0 = \frac{\omega}{c}$ is the wave vector of the propagating wave in vacuum. Equation (1.15) is known as the Helmholtz equation. This equation has to be solved separately in regions of constant ε, and the obtained solutions have to been matched using appropriate boundary conditions. Solving the Helmholtz equation in the propagation geometry of one-dimensional problem, which ε depends only on one spatial coordinate, yields the general analysis of guided electromagnetic modes in waveguides. Specifically, in cartesian coordinate system, the waves propagate along the x-direction and show no spatial variation in the perpendicular, in-plane y-direction. Therefore $\varepsilon = \varepsilon(\mathrm{z})$. Thus, propagating can be described as $\mathbf{E}(\mathrm{x}, \mathrm{y}, \mathrm{z}) = \mathbf{E}(\mathrm{z}) e^{i\beta x}$, where $\beta = k_x$ is called propagation constant. Inserting this expression into (1.15) yields the desired form of the wave equation

$$\frac{\partial^2 \mathbf{E}(\mathrm{z})}{\partial \mathrm{z}^2} + (\mathrm{k}_0^2 \varepsilon - \beta^2)\mathbf{E} = 0 \tag{1.16}$$

Solving this equation yields two sets of self-consistent solutions with different polarization properties of the propagating waves. The firs set are the transverse magnetic (TM) modes, where only the field components E_x, E_z, and H_y are nonzero, and the second set the transverse electric (TE) modes, with only H_x, H_z, and E_y being nonzero.

For TM modes, the system of governing equations are

$$E_x = -i\frac{1}{\omega\varepsilon_0\varepsilon}\frac{\partial H_y}{\partial z} \tag{1.17}$$

$$E_z = -\frac{\beta}{\omega\varepsilon_0\varepsilon}H_y \tag{1.18}$$

$$\frac{\partial^2 H_y}{\partial z^2} + (k_0^2\varepsilon - \beta^2)H_y = 0 \tag{1.19}$$

For TE modes, the analogous set is

$$H_x = i\frac{1}{\omega\mu_0}\frac{\partial E_y}{\partial z} \tag{1.20}$$

$$H_z = \frac{\beta}{\omega\mu_0}E_y \tag{1.21}$$

$$\frac{\partial^2 E_y}{\partial z^2} + (k_0^2\varepsilon - \beta^2)E_y = 0 \tag{1.22}$$

With these TM and TE modes equations, SPPs can be described.

The most simple geometry sustaining SPPs is that of a single, flat interface between a dielectric and an adjacent conducting half space. When the equations are solved with this boundary condition, the propagating wave solutions confined to the interface, with evanescent decay in the perpendicular z-direction, can be achieved for TM modes equations. However, there is no surface modes for TE polarization when the equations are solved for this boundary condition. SPPs only exist for TM polarization.

When there is a metal film sandwiched between two insulators, each single interface can sustain bound SPPs for TM modes. When the separation between adjacent interfaces is comparable to or smaller than the decay length of the surface mode, interactions between SPPs give rise to coupled modes. The general properties of coupled SPPs can be analyzed in a three-layer system with two boundary conditions as shown in Figure 1-1 [1].

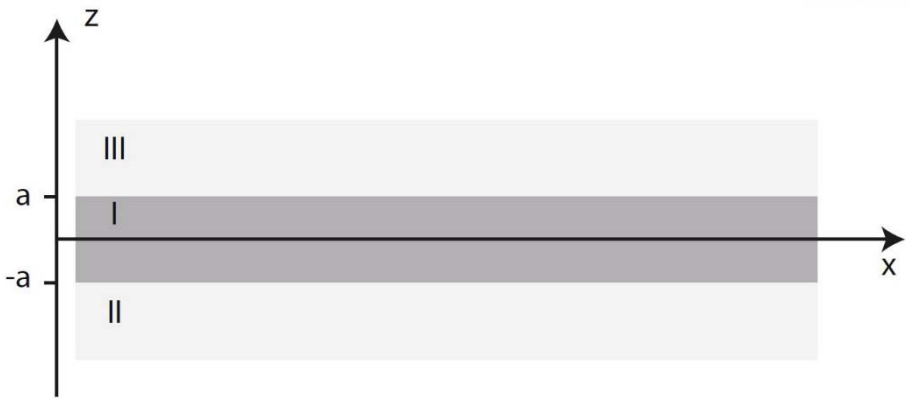

Figure 1-1. Geometry of a three-layer system consisting of a thin layer I (metal) sandwiched between two infinite half spaces II and III (insulator). [1]

Since there exist no modes for TE polarization, a general description of TM modes (1.17, 1.18, and 1.19) are only concerned. For z > ɑ, the field components are

$$H_y = Ae^{i\beta x}e^{-k_3 z} \tag{1.23}$$

$$E_x = iA\frac{1}{\omega\varepsilon_0\varepsilon_3}k_3 e^{i\beta x}e^{-k_3 z} \tag{1.24}$$

$$E_z = -A\frac{\beta}{\omega\varepsilon_0\varepsilon_3}e^{i\beta x}e^{-k_3 z} \tag{1.25}$$

while for z < - ɑ,

$$H_y = Be^{i\beta x}e^{k_2 z} \tag{1.26}$$

$$E_x = -iB\frac{1}{\omega\varepsilon_0\varepsilon_2}k_2 e^{i\beta x}e^{k_2 z} \tag{1.27}$$

$$E_z = -B\frac{\beta}{\omega\varepsilon_0\varepsilon_2}e^{i\beta x}e^{k_2 z} \tag{1.28}$$

where ε_i is the dielectric constant of the layer i and k_i is the component of the wave vector perpendicular to the interfaces simply as $k_i \equiv k_{z,i}$, for $i = 1, 2, 3$. It is clear that the fields decay

exponentially in the insulators (II) and (III).

In the core region - α < z < α, the modes localized at the bottom and top interface couple, yielding

$$H_y = Ce^{i\beta x}e^{k_1 z} + De^{i\beta x}e^{-k_1 z} \tag{1.29}$$

$$E_x = -iC\frac{1}{\omega\varepsilon_0\varepsilon_1}k_1 e^{i\beta x}e^{k_1 z} + iD\frac{1}{\omega\varepsilon_0\varepsilon_1}k_1 e^{i\beta x}e^{-k_1 z} \tag{1.30}$$

$$E_z = C\frac{\beta}{\omega\varepsilon_0\varepsilon_1}e^{i\beta x}e^{k_1 z} + D\frac{\beta}{\omega\varepsilon_0\varepsilon_1}e^{i\beta x}e^{-k_1 z} \tag{1.31}$$

The requirement of continuity of H_y and E_x results in an implicit expression for the dispersion relation linking β and ω ($\mathrm{k}_i^2 = \beta^2 - \mathrm{k}_0^2\varepsilon_i$, for $i = 1, 2, 3$) via

$$e^{-4k_1 a} = \frac{k_1/\varepsilon_1 + k_2/\varepsilon_2}{k_1/\varepsilon_1 - k_2/\varepsilon_2}\frac{k_1/\varepsilon_1 + k_3/\varepsilon_3}{k_1/\varepsilon_1 - k_3/\varepsilon_3} \tag{1.16}$$

Therefore, the SPPs properties at an insulator-metal-insulator (IMI) structure can be described. Especially, when the sub- and superstrates, (II) and (III), are equal in terms of their dielectric response, two different coupled SPP modes exist; long-range SPP (LRSPP) and short-range SPP (SRSPP). The LRSPP have the interesting property that upon decreasing metal film thickness, the confinement of the coupled SPP to the metal film decreases as the mode evolves into a plane wave supported by the homogeneous dielectric environment and the propagation length of the LRSPP increases drastically. However, when the sub- and superstrates have different dielectric constants, LRSPP cannot exist in this three-layer system. On the other hand, the SRSPP exhibit the opposite behavior – their confinement to the metal increases with decreasing metal film thickness, resulting in a reduction in propagation length. In addition, the SRSPP can exist even when two insulators have different dielectric response in this three-layer system.

In this thesis, the SRSPP is the major concern due to its confinement to the metal. To achieve an extreme confinement, the SRSPP in an ultrathin metal film and metal strips is investigated.

1.2. Short-range surface plasmon polariton in an ultrathin metal film

Ultrathin metal film has been widely studied due to its characteristics; transparency in the visible and extreme mode confinement with large propagation constant.

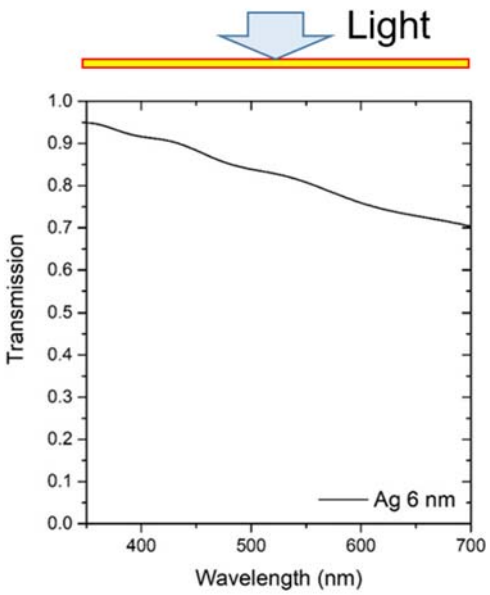

Figure 1-2. The transmission spectrum of the 6-nm-thick Ag film when light is incident vertically. Calculated with the finite difference time domain (FDTD) method (FDTD Solutions, Lumerical Inc.)

Ultrathin metal film which thickness is thinner than the penetration depth has high transparency in visible regime. When a wave is incident on a metal, the magnitude of the wave decays exponentially from the surface of the metal. This decay length is called the penetration depth, and almost wave is reflected at the metal surface. However, when a metal thickness is thinner than the penetration depth, a wave can pass through the metal. Especially, when a metal thickness is less than tens of nanometers, metal is almost transparent in visible range. Figure 1-2 shows the transmission spectrum of 6-nm-thick Ag film in visible range. The transmission is over than 70 % in all visible range.

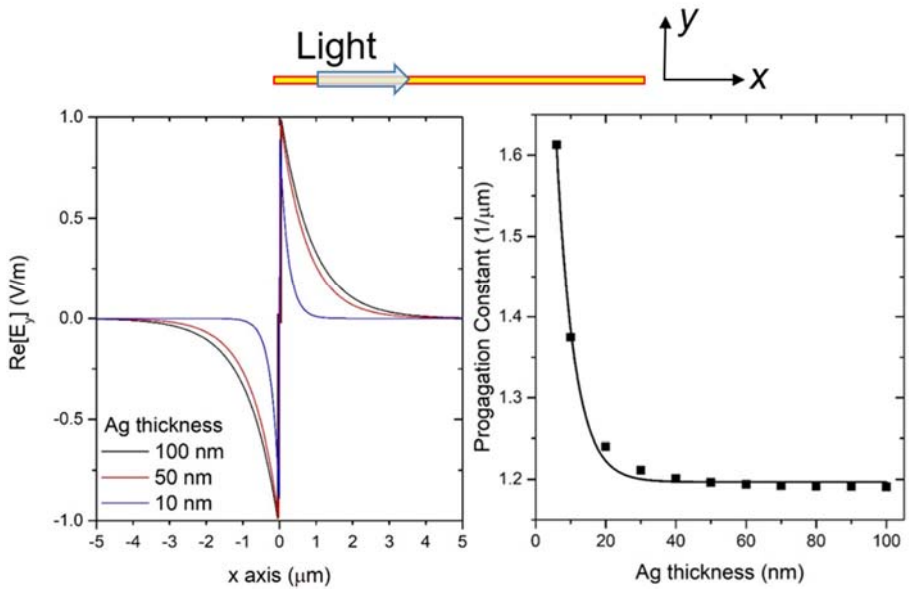

Figure 1-3. (a)The E_y field distribution and (b) the propagation constant of the short-range surface plasmon polariton of a wavelength 850 nm propagating along the ultrathin metal film. Calculated with the finite difference time domain (FDTD) method (FDTD Solutions, Lumerical Inc.)

In addition, short-range surface plasmon polaritons (SRSPPs) can be excited at a metal film with the proper techniques such as grating coupling, prism coupling and so on. An SRSPP is a wave which propagates along a metal surface and its electric field is confined around a metal film [2]. When an ultrathin metal film exists, the electric field of the SRSPP mode can be confined in extremely narrow region and its propagation constant increases as shown in Figure 1-3.

There are many devices based on an ultrathin metal film such as plasmonic color filters [3-5], visible light modulators [6], and metasurfaces [7]. In this thesis, a modulator consists of ultrathin metal film and metal strip array for a wavelength 850 nm has been studied.

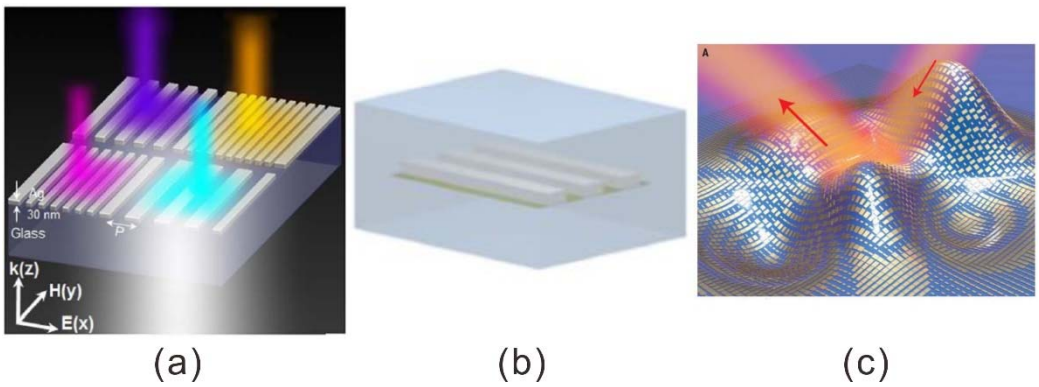

Figure 1-4. Examples of the devices based on an ultrathin metal film. (a) Plasmonic color filter [3], (b) visible light modulator [6], and (c) metasurfaces [7].

1.3. Localized surface plasmon resonance in a thin metal strip

When a p-polarized light is incident on a metal strip array which thickness is thinner than the penetration depth, an SRSPP is excited around a metal strip. This SRSPP propagates forwards and backwards along the strip, and the strip behaves like the Fabry-Perot (FP) resonator [8-11].

A typical FP resonator consists of two parallel optical mirrors. The light propagating in one direction in the FP resonator is reflected backwards when it is incident on a mirror. Then, the reflected light propagates backwards, and it is reflected again when it is incident on another mirror. Reflected light from the mirrors interfere constructively and give rise to a resonance mode. The resonance wavelength λ_r is determined by the FP relation of the FP resonator. Similarly, in a metal strip, the two strip edges behave as optical mirrors. Therefore, it has the resonance mode. The FP relation in a metal strip is,

$$\frac{2\pi}{\lambda_r} N_s w + \varphi = m\pi \tag{2}$$

where λ_r is a resonance wavelength, N_s is the effective index of the SRSPP, and φ is the phase change caused by the reflection of the SRSPP at the edge of the strip.

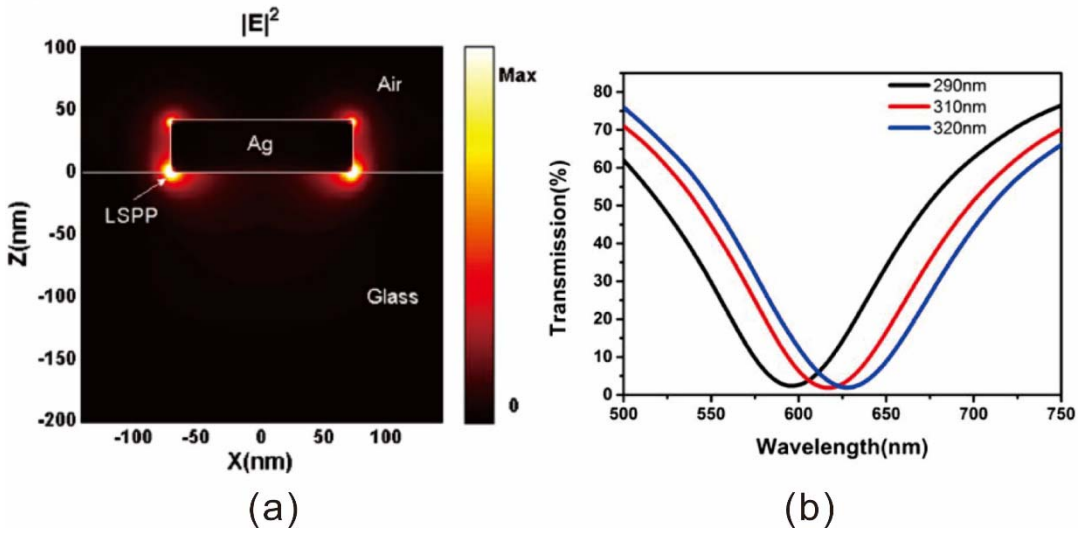

Figure 1-5. Example of the localized surface plasmon resonance around a thin metal strip (a) and the transmission spectrum with the rejection band (b) [4].

In a thin metal strip, the excited SRSPP which travels back and forth along the metal strip has the resonance mode, the localized surface plasmon resonance (LSPR). Figure 1-5 (a) shows the LSPR around a thin metal strip. Then, the directly transmitted light and the scattered light due to the LSPR have destructive interference [12-17]. Therefore, there exists a rejection band in transmission spectrum as shown in Figure 1-5 (b).

1.4. Properties of infrared wireless communication

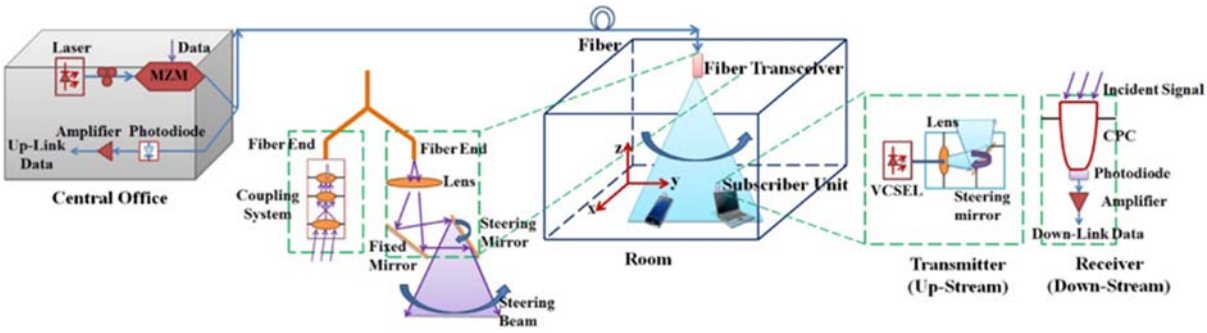

Figure 1-6. Example of infrared (IR) wireless communication systems [18].

Infrared (IR) wireless communications have huge merits such as broadband optical wireless communication and unregulated bandwidth without electromagnetic interference. Therefore, IR wireless communications have been widely studied, such as indoor localization systems [18] and light fidelity (Li-Fi) [19]. However, their modulation bandwidth is limited since they are based on intensity modulation with direct detection. Thus, the direct switching speed of the IR sources controls modulation bandwidth of IR wireless communications.

There are two major sources of IR wireless communications; light emitting diodes (LEDs) and vertical cavity surface emitting lasers (VCSELs). Although LEDs can be used as low-cost sources of wireless communications, it has low modulation bandwidth which is limited to 10 MHz. In addition, LEDs also have a nonlinearity problem. On the other hand, VCSELs can have high modulation bandwidth which is up to 1 GHz. However, the cost for VCSELs is more expensive than that of LEDs. Therefore, indirect modulation using an external modulator is needed to have large modulation bandwidth and to remove the nonlinearity problem.

As the detection of light sources, low-cost silicon p-i-n photodetectors are widely used. The responsivity peak of those photodetectors is in the range of 850 nm to 950 nm. In this thesis, a modulator for a wavelength 850 nm LED is studied. For modulation, indium-tin-oxide (ITO), one of the transparent conducting oxides (TCOs), is used as a semiconductor in metal-oxide-semiconductor (MOS) capacitor structure. The characteristics of geometric parameters of the proposed modulator and intensity modulation have been investigated. By applying a bias voltage 46 V, almost 200 % transmission is increased compared to non-bias state at λ_r = 850 nm. A simple thin metal strip array patterns, subtractive color filters, have been experimented as a preliminary experiment of a future realization of the proposed modulator.

II. Optical and electrical characteristics of the proposed modulator

2.1. Proposed modulator for IR wireless communications

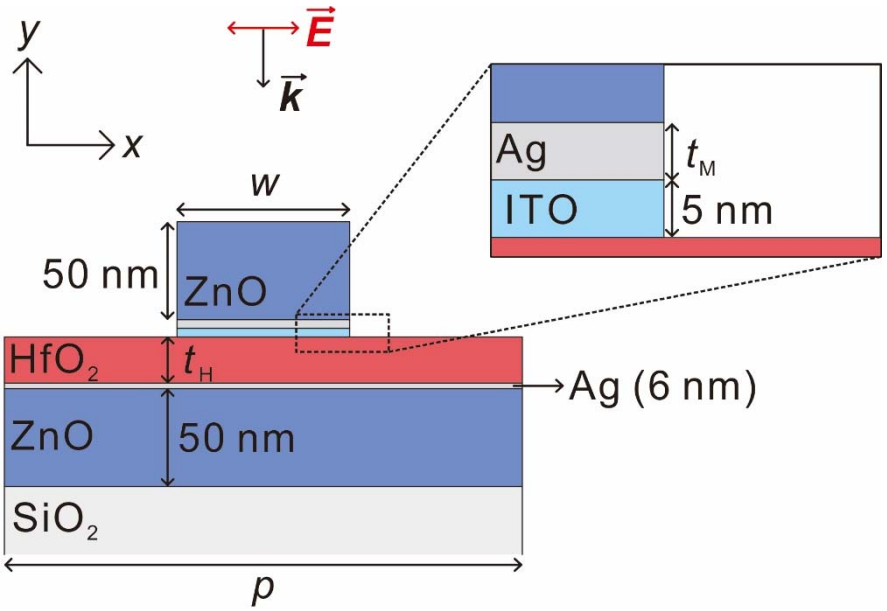

Figure 2-1. Unit cell structure of the proposed modulator.

The unit cell structure of the proposed modulator is schematically shown in Figure 2-1. It is uniform in the z direction and repeated in the x direction with a period p. The unit cell consists of a stack of zinc oxide (ZnO), Ag, and hafnium oxide (HfO_2) layers on a silicon dioxide (SiO_2) substrate and another stack of indium-tin-oxide (ITO), Ag, and ZnO strips of width w on the layer stack. The 50-nm-thick lower ZnO layer of the layer stack is required to obtain the continuous 6-nm-thick Ag layer on it in a future realization process, since the direct adhesion between Ag layer and SiO_2 substrate is poor. The Ag layer on the ZnO layer functions as a transparent electrode. The HfO_2 layer with a thickness t_H is the oxide of the metal-oxide-semiconductor (MOS) structure. The ITO strip is 5 nm thick and the Ag strip has a thickness t_M. The 50-nm-thick ZnO strip is used to prevent the Ag strip from being oxidized.

When a p-wave is incident on the modulator from the top, a sort of short-range surface plasmon polariton (SRSPP), which is strongly confined around the Ag strip, is excited and it travels back and forth along the strip in the x direction. In consequence, the strip behaves like a Fabry-Perot (FP) resonator and it has the localized surface plasmon resonance (LSPR). The destructive interference between the light directly transmitted across the strip array and the light radiated from the LSPR causes the rejection band in the transmission spectrum of the structure.

In this thesis, simple MOS capacitor structure is used to achieve modulation of the rejection band in the transmission spectrum. The MOS capacitor consists of Ag, HfO_2 layer, and ITO strip. If a voltage is applied between the Ag layer and the Ag strip, the refractive index of ITO changes. Then, the SRSPP wavelength around the Ag strip is shifted due to the change of the effective index of the SRSPP. Therefore, the modulation of the rejection band can be achieved.

2.2. Properties of indium-tin-oxide (ITO)

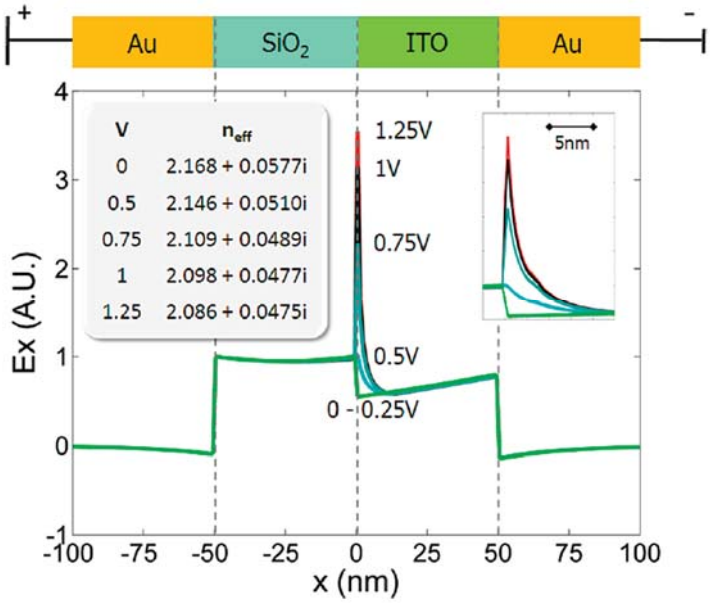

Figure 2-2. Example of electric field distribution as function of applied voltage. [20].

Transparent conducting oxide (TCO) is doped metal oxide which is optically transparent and electrically conductive. By using the MOS structure, the carrier concentration of TCO can be controlled when there is a voltage between the metal and the semiconductor. Since the refractive index of TCO is affected by the carrier concentration of TCO, it can be adjusted by applying the bias voltage. Figure 2-2 shows the electric field distribution as function of applied voltage. When there is an applied voltage, the TCO carrier concentration changes such that the TCO optical properties are adjusted. This results in the different electric field according to the applied voltage. the majority carriers are accumulated or depleted on the semiconductor side at the interface between the oxide and the semiconductor of the MOS structure.

The relation between the carrier concentration and the dielectric constant can be analyzed with the Drude model. The Drude model is,

$$\varepsilon(\omega) = \varepsilon_\infty - \frac{\omega_p^2}{\omega^2 + i\gamma\omega} \tag{3}$$

where ε_∞ is high frequency permittivity, $\omega_p^2 = \frac{ne^2}{\varepsilon_0 m_{eff}}$ is the plasma frequency of the free electron gas, and $\gamma = \frac{e}{\mu m_{eff}}$ is collision frequency. The Drude model of the optical response of metals is also known as the dielectric function of the free electron gas. In other words, the dielectric function of the electron concentration can be calculated by the Drude model [1].

In this thesis, ITO, one of the TCO materials, is used. When the refractive index of the ITO strip is adjusted, the LSPR wavelength is also adjusted since the effective index of LSPR mode is changed. The ITO strip is set to 5-nm-thick to achieve larger modulation with the consideration of the LSPR field distribution.

In addition, in MOS capacitor, if oxide has high relative dielectric permittivity, small driving voltage can make big electric field between metal and semiconductor. Thus, more carriers can be accumulated in semiconductor region when the same voltage is applied with high-k oxide. For instance, HfO_2 has the relative permittivity of 25 and SiO_2 has the relative permittivity of 3.9. Therefore, the high-k material, HfO_2 is used as the insulator for efficient modulation.

2.3. Characteristics of the proposed structure

To analyze the optical properties of the modulator, the finite difference time domain (FDTD) method (FDTD Solutions, Lumerical Inc.) is used. The period boundary condition is applied to the left and right boundaries, and perfectly matched layers are placed on the upper and lower boundaries of the structure in Figure 2-1. A p-wave is incident at an angle θ to the y-axis, and the transmission is monitored in the SiO_2 substrate. In addition, the reflection from the modulator is monitored above the strip stack. The pulse width of the p-wave is chosen such that the transmission is calculated in the wavelength interval between 350 nm and 1,000 nm, for the investigation of the modulator at the wavelength 850 nm and the preliminary experiment in visible range in Section Ⅲ. The optical constants of SiO_2 and HfO_2 are taken from [21] and [22], respectively. The dielectric constants of Ag and ZnO are measured with ellipsometry.

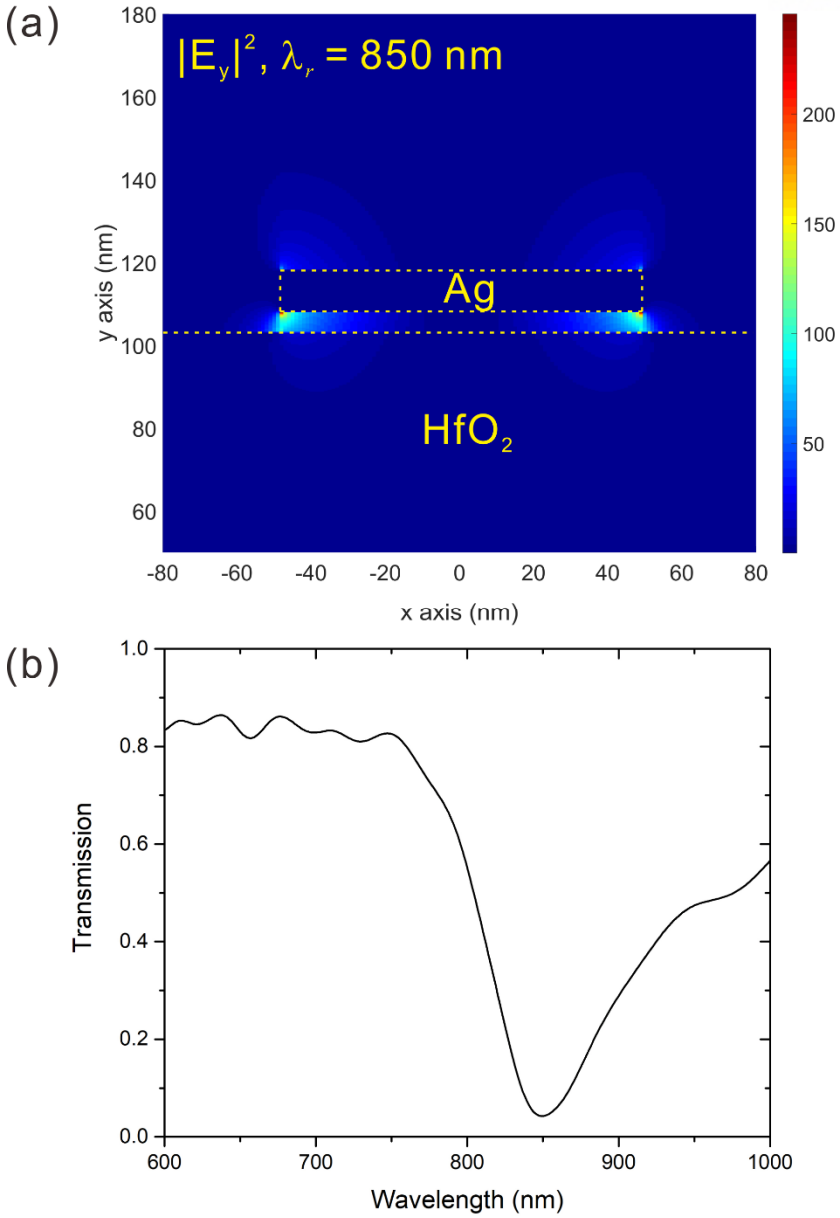

Figure 2-3. Electric field and the transmission spectrum of the proposed modulator when w = 97 nm, p = 291 nm (3w), t_M = 10 nm, t_H = 100 nm, and θ = 0°. (a) The $|E_y|^2$ field at λ_r = 850 nm and (b) the rejection band caused by the LSPR in transmission spectrum at λ_r = 850 nm.

Figure 2-3 shows the E_y field distribution and transmission spectrum of the modulator without a voltage to the modulator. When w = 97 nm, p = 291 nm (3w), t_M = 10 nm, t_H = 100 nm, and θ = 0°, the LSPR is located at λ_r = 850 nm as shown in Figure 2-3(a). This LSPR causes the rejection band at the resonance wavelength, 850 nm (Figure 2-4(b)). Transmission is higher than 80 % out of the rejection band, since the Ag layer is 6-nm-thick, an ultrathin metal film. The minimum transmission at the resonance wavelength λ_r = 850 nm is 4 %.

2.4. Influence of geometrical parameters

The excitation condition of the SRSPP can be differed by the structure geometry. Therefore, to obtain proper geometric value of the modulator, each geometrical parameter such as period p, strip width w, strip thickness t_M, oxide thickness t_H, and incident angles are investigated.

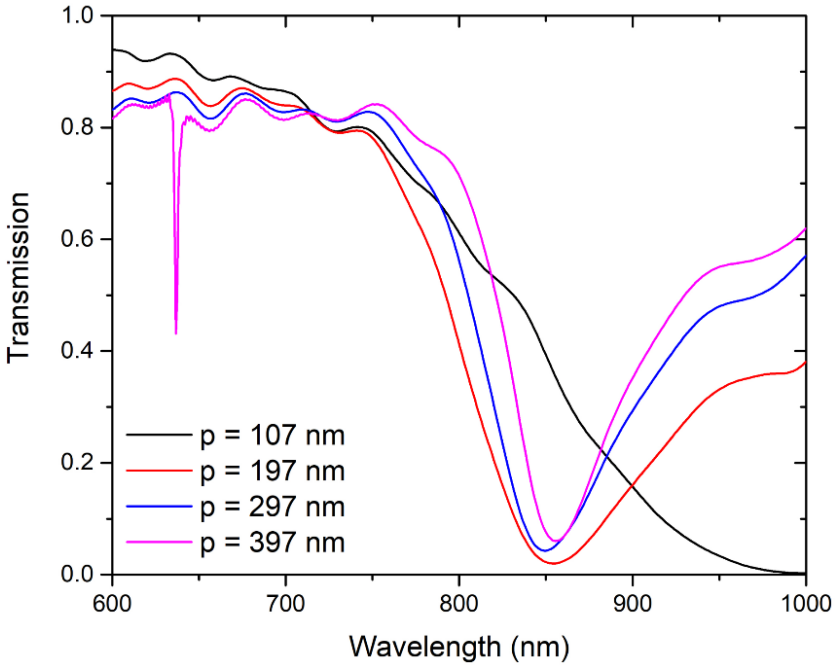

Figure 2-4. Influence of the period p of the proposed modulator.

Figure 2-4 shows the influence of the period p, while other parameters are $w = 97$ nm, $t_M = 10$ nm, $t_H = 100$ nm, and $\theta = 0°$. Since strips are too closely located when the period $p < 3w$, the LSPR around one Ag strip is coupled to other LSPRs. It results in broadened bandwidth and shifts of the rejection band. On the other hand, if $p > 3w$, the minimum transmission of the rejection band increases. Therefore, the period p is set to $3w$ to excite LSPR without coupling and to have moderate bandwidth.

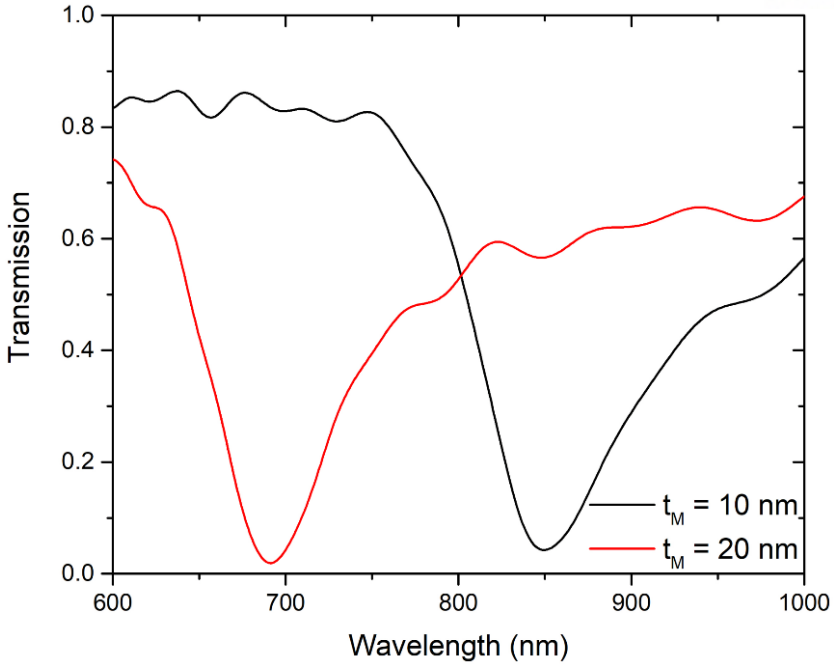

Figure 2-5. Influence of the strip thickness t_M of the proposed modulator.

Figure 2-5 shows the influence of the strip thickness t_M, while other parameters are w = 97 nm, p = 3w, t_H = 100 nm, and θ = 0°. This can be explained with the FP resonance relation, equation (2). As t_M decreases, the effective index N_s increases such that the resonance wavelength λ_r increases. The effective index of SRSPP with the different strip thickness is shown in Figure 2-6.

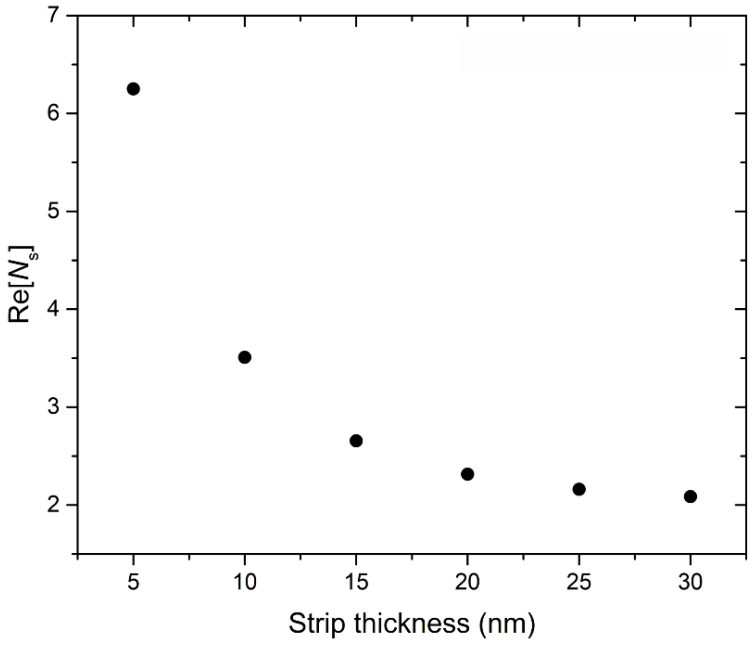

Figure 2-6. The effective index of SRSPP at the different strip thickness.

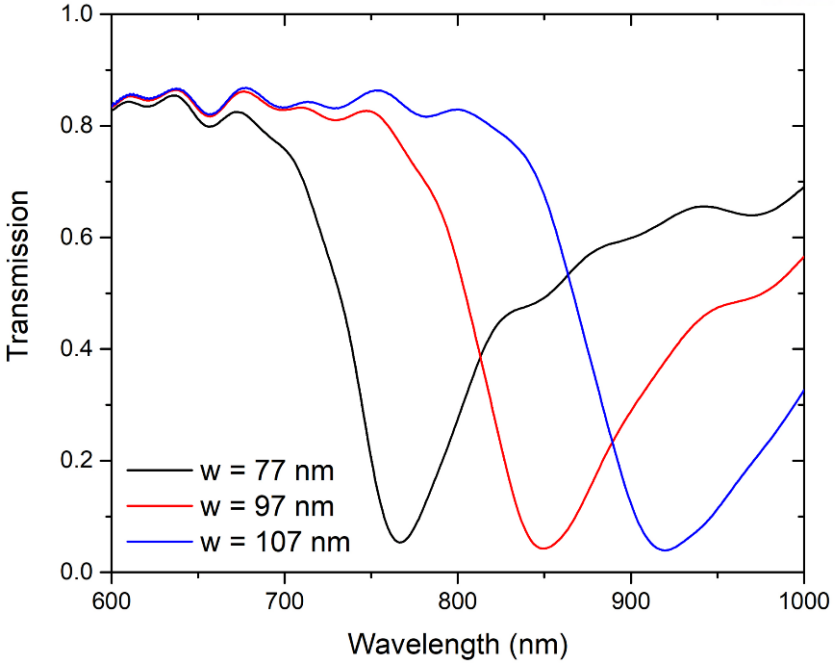

Figure 2-7. Influence of the strip width w of the proposed modulator.

Similarly, the influence of the strip width as shown in Figure 2-7 also can be explained with the FP relation. Other parameters are $p = 3w$, $t_M = 10$ nm, $t_H = 100$ nm, and $\theta = 0°$. From the equation (2), the resonance wavelength λ_r increases with the strip width w increases. Because the resonance wavelength increases (decreases) when propagating distance of the wave in the resonator, the strip width, increases (decreases).

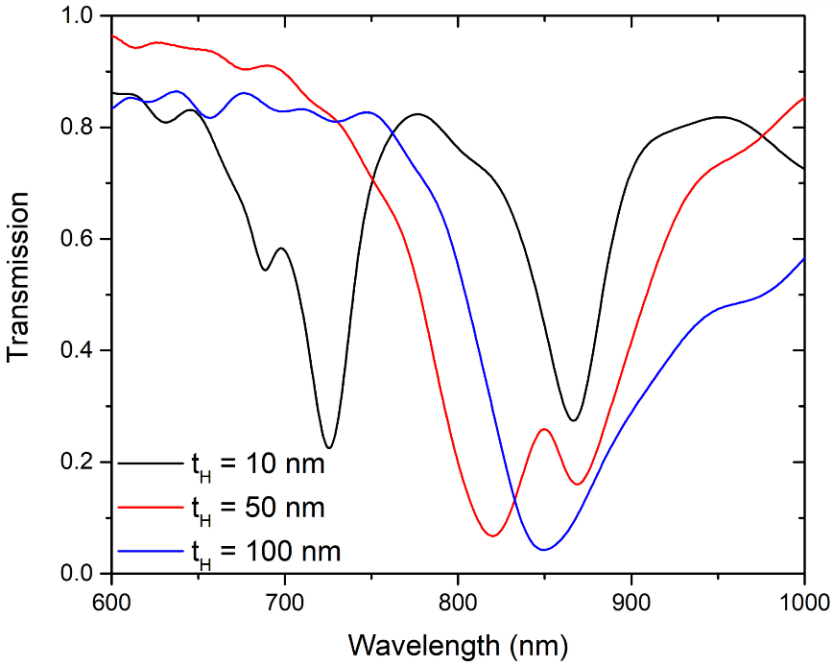

Figure 2-8. Influence of the oxide thickness t_H of the proposed modulator.

Figure 2-8 shows the influence of the oxide, the insulator, thickness. When the insulator thickness smaller than 100 nm, while other parameters are w = 97 nm, p = 3w, t_M = 10 nm, and θ = 0°, the resonance dip diverges into two resonance dips. And, the minimum transmission increases.

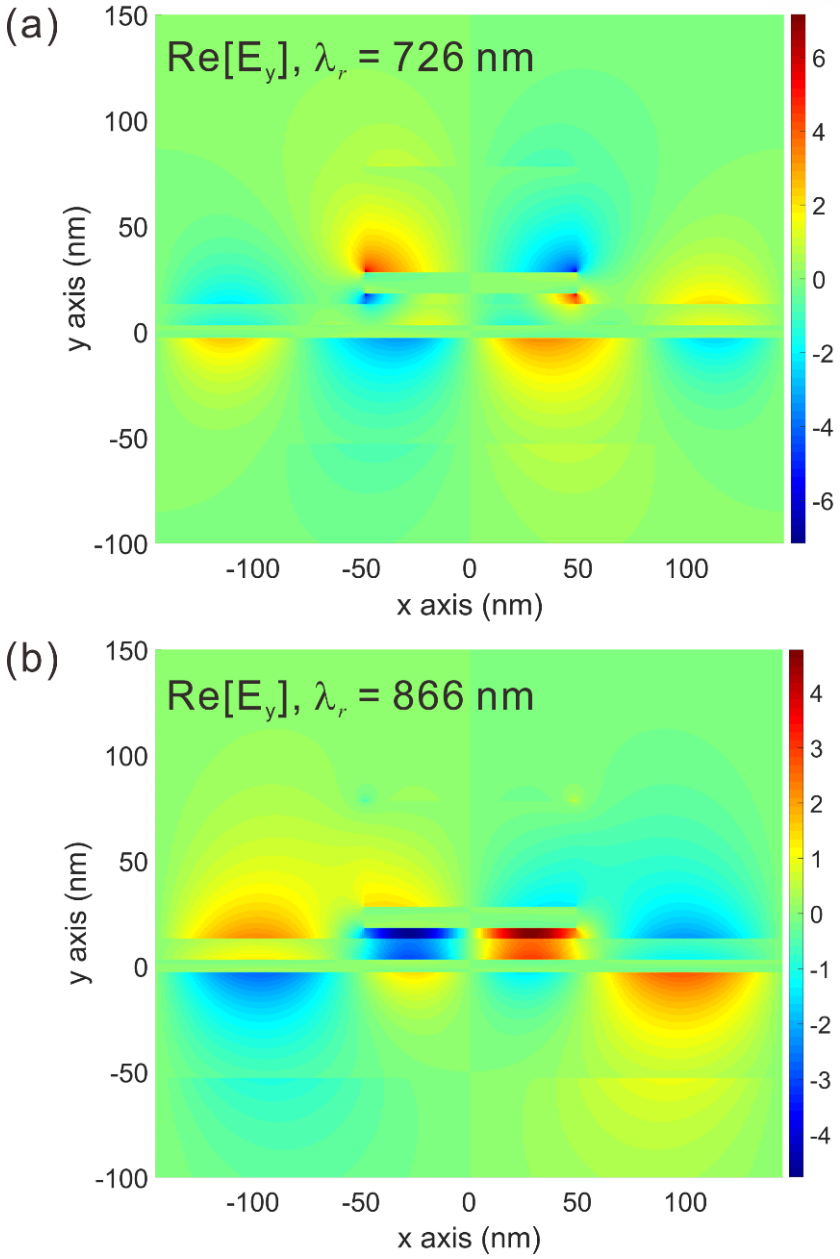

Figure 2-9. The E_y field of the two resonance dips when w = 97 nm, p = 291 nm (3w), t_M = 10 nm, t_H = 10 nm, and θ = 0°. (a) The E_y field distribution at λ_r = 726 nm and (b) the E_y field distribution at λ_r = 866 nm.

Figure 2-9 shows the vertical electric field component of the two diverged dips when t_H = 10 nm. In Figure 2-9 (a) and (b), E_y field is distributed around both the Ag strip and the Ag layer. Because as the insulator thickness t_H decreases, strong interaction between the Ag strip and the Ag layer exists. Since the LSPR is not well confined around the Ag strip, the destructive interference between the incident wave and the scattered wave due to the LSPR reduces. In consequence, the transmission at the resonance increases.

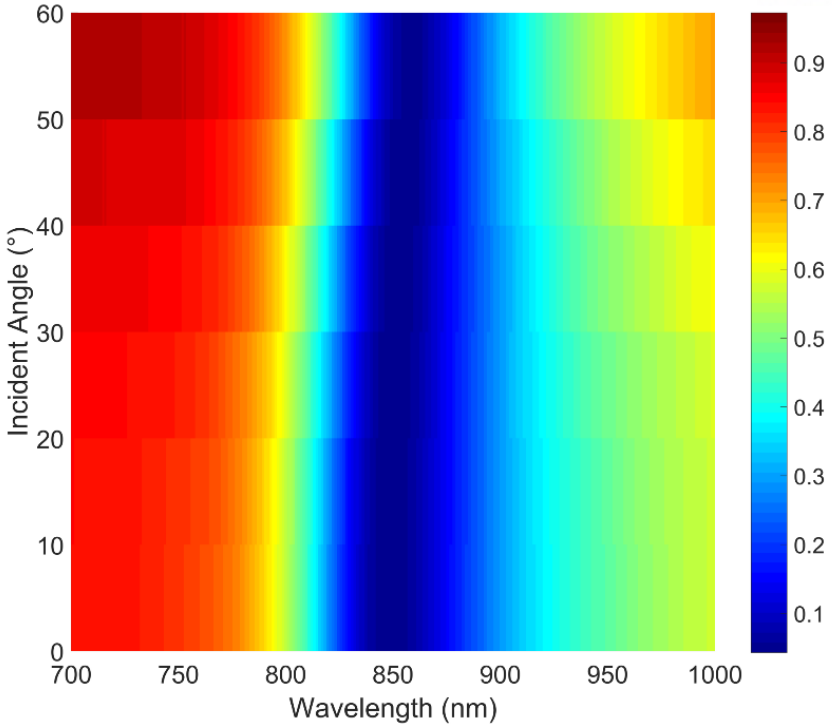

Figure 2-10. Influence of the incident angle of the proposed modulator.

The transmission spectrum with incident angle from 0° to 60° is shown in Figure 2-10 when other parameters are w = 97 nm, p = 3w, t_M = 10 nm, and t_H = 100 nm. If the SRSPP is excited due to the grating structure of the modulator, it should satisfy the grating coupling condition: $k_{spp} = k_0 sin\theta + mG$, where k_{spp} is the coupled SPP wave vector, k_0 is vacuum wave vector, m is an integer, G is $2\pi/\Lambda$, and Λ is a period of the grating. Thus, the coupled SPP wavelength should change when incident angle increases. However, in this thesis, since the LSPR causes the rejection band, the resonance wavelength does not change when the incident angle is smaller than 60°.

2.5. Electrically tunable ITO refractive index

To analyze the electrical properties of ITO, DEVICE simulation tool (DEVICE, Lumerical Inc.) is used. The electrical properties of Ag and HfO_2 are applied from the database of the DEVICE. ITO electrical property is taken from the [23]. With the same structure in Figure 2-1, the periodic boundary condition is applied to the left and the right boundaries, and closed boundary condition is applied to the upper and lower boundaries. The voltage from 0 V to 46 V is applied to the Ag layer and the voltage of the Ag strip is set to 0 V. And the ITO is doped with n-type carrier with the doping concentration $N_0 = 1 \times 10^{19}$ cm^{-3}. If the initial doping rate is higher than N_0, the ITO has different refractive index from the low-doped ITO state, due to the closer plasma frequency to the wavelength 850 nm. While, the initial doping rate is lower than N_0, larger voltage is required to increase the carrier concentration. The Fermi statistics is applied in charge solvers in DEVICE simulation, since ITO is degenerately doped, N_0.

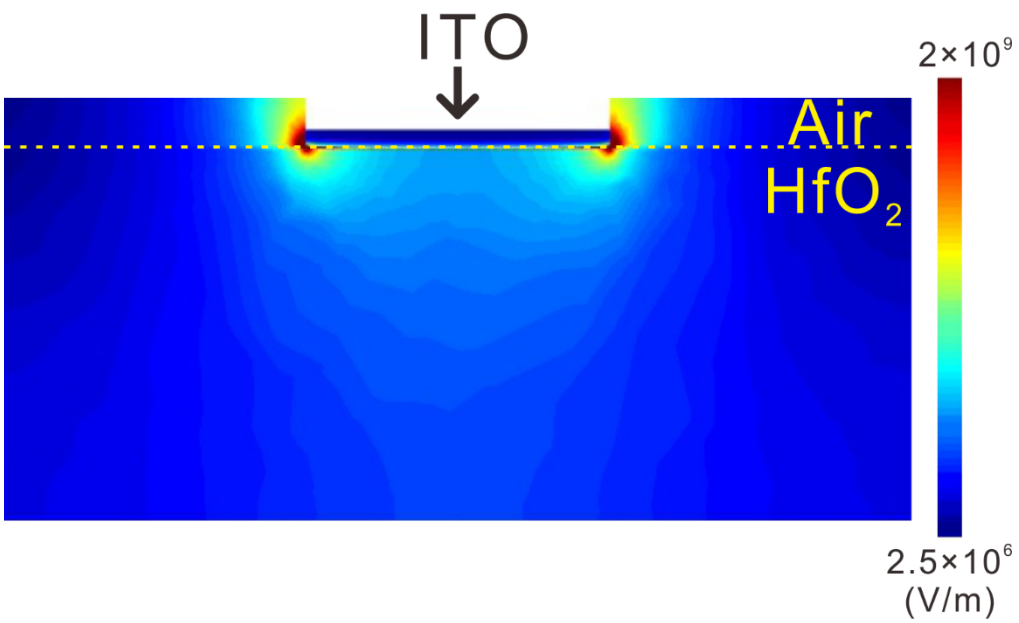

Figure 2-11. The electric field distribution of the proposed modulator in DEVICE simulation (Lumerical Inc.). The yellow dashed line is the edge of the HfO_2, and the Ag strip and the Ag layer are not indicated in the figure.

The proposed modulator is not a perfect parallel MOS capacitor. Thus, when there is a bias voltage between the Ag strip and the Ag layer, there exists a strong fringing electric field. It results in the strong electric field at the edge of the ITO strip as shown in Figure 2-11.

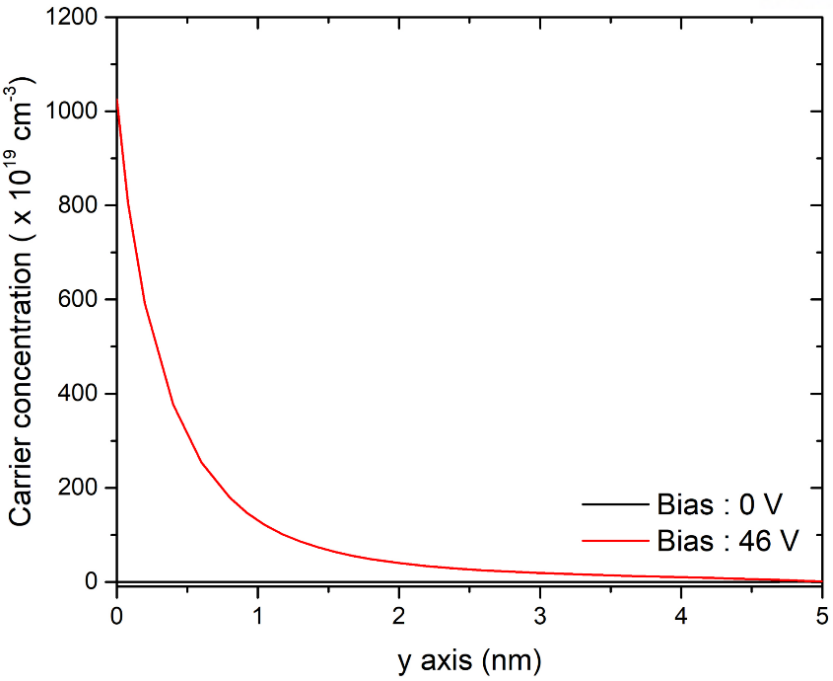

Figure 2-12. The carrier concentration distribution of the ITO strip when there is a bias voltage between the Ag strip and the Ag layer. The interface between HfO_2 and ITO is at y = 0. The carrier concentration is indicated in black solid line (0 V bias) and red solid line (46 V bias).

Due to this strong electric field, the ITO carrier concentration at the edge of the strip can be increased up to $N = 1 \times 10^{22}$ cm^{-3} at the interface between HfO_2 and ITO as shown in Figure 2-12. By increasing the bias voltage from 0 V to 46 V, the carrier concentration at the edge of the ITO surface can be increased from $N_0 = 1 \times 10^{19}$ cm^{-3} to $N = 1 \times 10^{22}$ cm^{-3}. In the middle region of the ITO surface, however, the carrier concentration increases to $N = 1.15 \times 10^{21}$ cm^{-3} at the bias voltage 46 V. To make the carrier concentration up to $N = 1 \times 10^{22}$ cm^{-3} at the middle of the ITO surface, much larger voltage is required. In addition, when the ITO strip is substituted with ITO layer, there are no regions which the carrier concentration can increase to $N = 1 \times 10^{22}$ cm^{-3} since there is no fringing electric field. This requires further study.

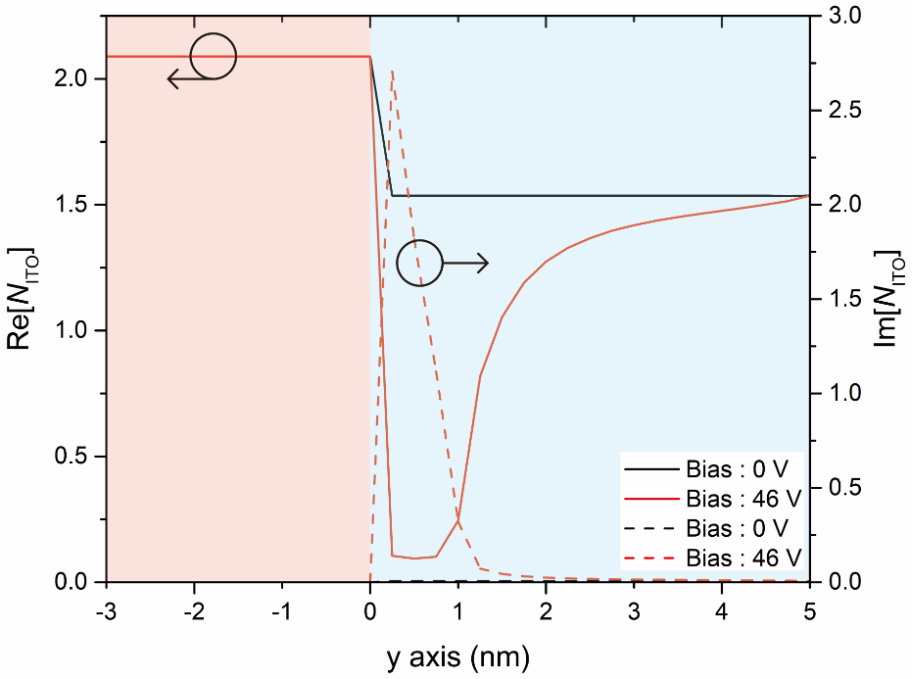

Figure 2-13. The change of the ITO strip refractive index according to the change of the carrier concentration in the ITO strip. The red region HfO_2 and the blue region is ITO. The Re[N_{ITO}] is indicated in solid lines and the Im[N_{ITO}] is indicated in dashed lines.

These change of carrier concentration in the ITO strip causes the change of the ITO strip refractive index. Figure 2-13 shows the change of the ITO strip refractive index. Significant refractive index changes occur at the edge of the ITO strip surface. The Re[N_{ITO}] decreases about 1.4 and the Im[N_{ITO}] increases about 2.7. The refractive index at the middle of the ITO surface decreases 0.5 in Re[N_{ITO}] and increases 0.1 in Im[N_{ITO}]. These results are calculated by the Drude model, equation (3). Since the refractive index has changed, the effective index of the LSPR mode also changes. Therefore, the resonance mode will change.

To increase the carrier concentration, large bias voltage (46 V) is required. The insulator HfO_2 is required to have larger breakdown voltage. The bias voltage 46 V in 100-nm-thick HfO_2 is the electric field of 4.6 MV/cm^{-1}, which is below the maximum breakdown field of HfO_2 film of 12 – 16 MV/cm^{-1} [24]. In addition, deposition of 100-nm-thick HfO_2 is possible with a technique called high target utilization sputtering [25].

2.6. Intensity modulation at 850 nm

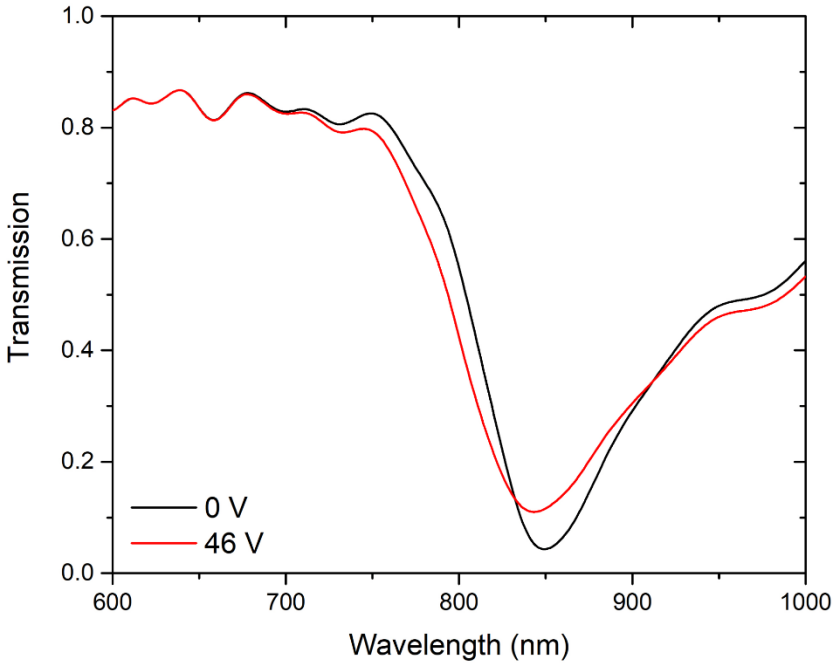

Figure 2-14. The transmission spectrum when there is a bias voltage between the Ag strip and the Ag layer. The black solid line is when the bias voltage V = 0 V, and the red solid line is when the bias voltage V = 46 V.

The transmission spectrum is calculated when there is a bias voltage 46 V between the Ag strip and the Ag layer (on-state), and when there is no bias voltage 0 V (off-state). Figure 2-14 shows the calculated transmission spectra when w = 97 nm, $p = 3w$, t_M = 10 nm, t_H = 100 nm, and $\theta = 0°$. At off-state, the LSPR causes the rejection band at λ_r = 850 nm with the minimum transmission 4 %. When off-state changes to on-state, almost 200 % transmission increase at λ_r = 850 nm, with blue-shift of the rejection band by 5 nm. This is resulted from the change of the ITO refractive index. The electric field of the LSPR, the resonance of the SRSPP, is strongly confined around the Ag strip. Thus, the effective index of SRSPP mode changes when the refractive index of the ITO changes. By applying bias of 46 V, the real part of the refractive index of the ITO strip changes from 1.5 to 0.1 and the imaginary part of the refractive index of the ITO increases from 0 to 2.7 at the HfO_2-ITO interface (Figure 2-13). Even though the SRSPP electric field around the Ag strip decays rapidly, the change of the ITO refractive index affects the effective index of SRSPP since the ITO strip is only 5 nm thick. Therefore, the modulated transmission spectrum has larger transmission value at λ_r = 850 nm and blue-shift of the rejection band.

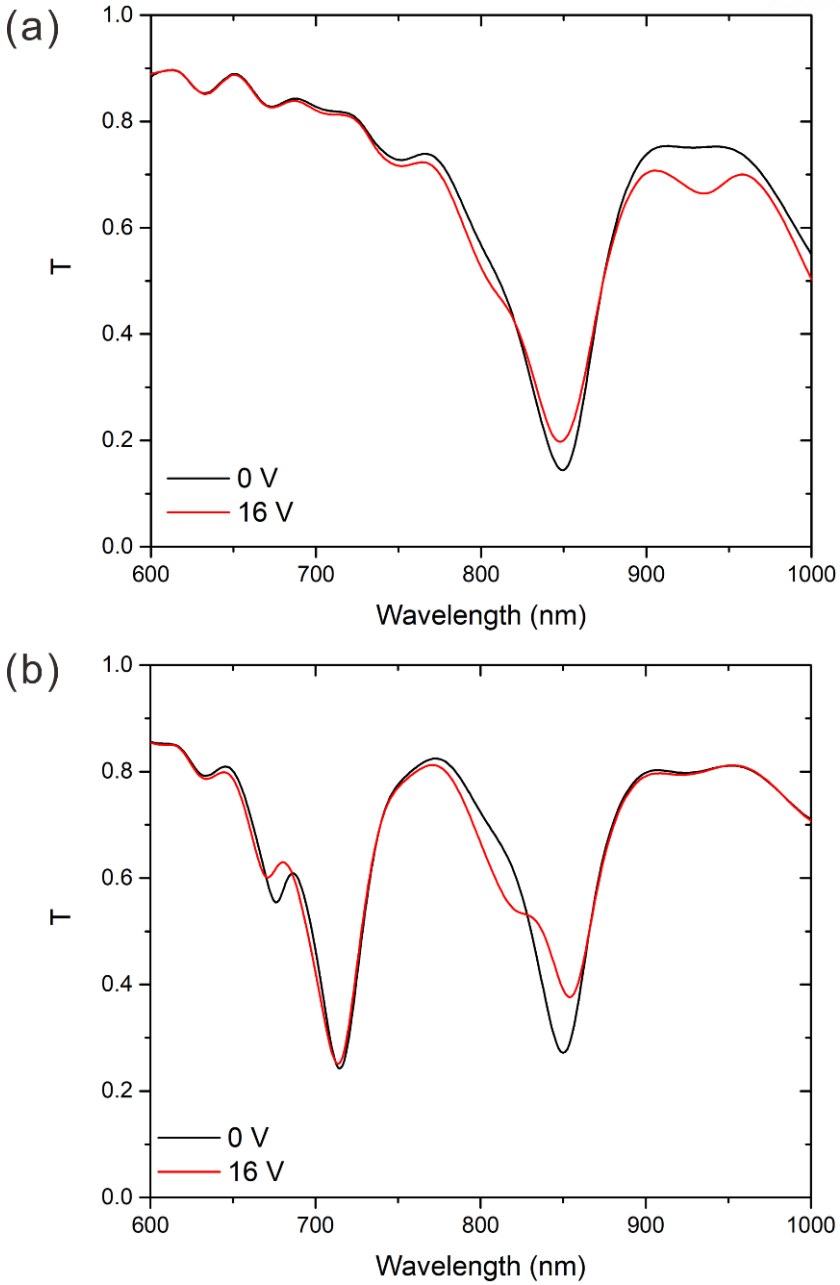

Figure 2-15. The transmission spectrum when there is a bias voltage between the Ag strip and the Ag layer. (a) the intensity modulation when w = 148 nm, p = 444 nm (3w), t_M = 10 nm, t_H = 10 nm, and θ = 0°, and (b) the intensity modulation when w = 93 nm, p = 279 nm (3w), t_M = 10 nm, t_H = 10 nm, and θ = 0°

To reduce the bias voltage 46 V, intensity modulation with smaller t_H is also investigated. Since there are two resonance dips when t_H = 10 nm, each resonance dip is located at 850 nm by adjusting the strip width w. Figure 2-15 shows the calculated transmission spectrum when the left-hand side dip is located at 850 nm (w = 148 nm) in Figure 2-15 (a) and the right-hand side dip is located at 850 nm (w = 93 nm) in Figure 2-15 (b), other parameters are remained the same. To compare modulation efficiency, the bias voltage is increased to 16 V where the carrier concentration of the ITO strip N = 1×10^{22} cm^{-3}. Compared

to t_H = 100 nm case, t_H = 10 nm structure requires smaller driving voltage to accumulate the same amount of carrier, since electric field between the Ag strip and the Ag layer is increased by reducing the thickness t_H when there is a bias voltage. However, because of the strong interaction between the Ag strip and the Ag layer, the off-state transmission of the rejection band is increased. In addition, intensity modulation is not efficient due to the distribution of electric field both the Ag strip and the Ag layer. When off-state changes to on-state, the transmission increases by 5.5 % when w = 148 nm (Figure 2-15 (a)) and 12 % when w = 93 nm (Figure 2-15 (b)) at λ_r = 850 nm.

The modulator for a wavelength 850 nm is investigated. With the 100-nm-thick insulator, the transmission increases 200 % at λ_r = 850 nm when there is an applied voltage 46 V between the Ag layer and the Ag strip. Although the modulation bandwidth of the proposed modulator is required to be investigated, the modulator is expected to have fast response than the direct modulation of light sources since the modulation bandwidth is determined either RC time constant or carrier transit time. In addition, the proposed modulator can be used directly on light sources. Because the device is transmissive modulator because of the use of ultrathin Ag layer and strip. This work has a great potential as an external modulator in near IR wireless communications.

III. Preliminary experiment

3.1. Fabrication of metal strip array

As a preliminary step before the fabrication of the proposed modulator, metal strip array on SiO_2 substrate is fabricated and experimented. This preliminary fabrication and experiment is necessary for the future realization of the proposed modulator. The optical characteristics of the proposed modulator can be verified by comparing the experiment and the simulation results of simple metal strip array on SiO_2 substrate. For this purpose, 2-nm-thick Cr and 18-nm-thick Au strip array on fused silica substrate is fabricated.

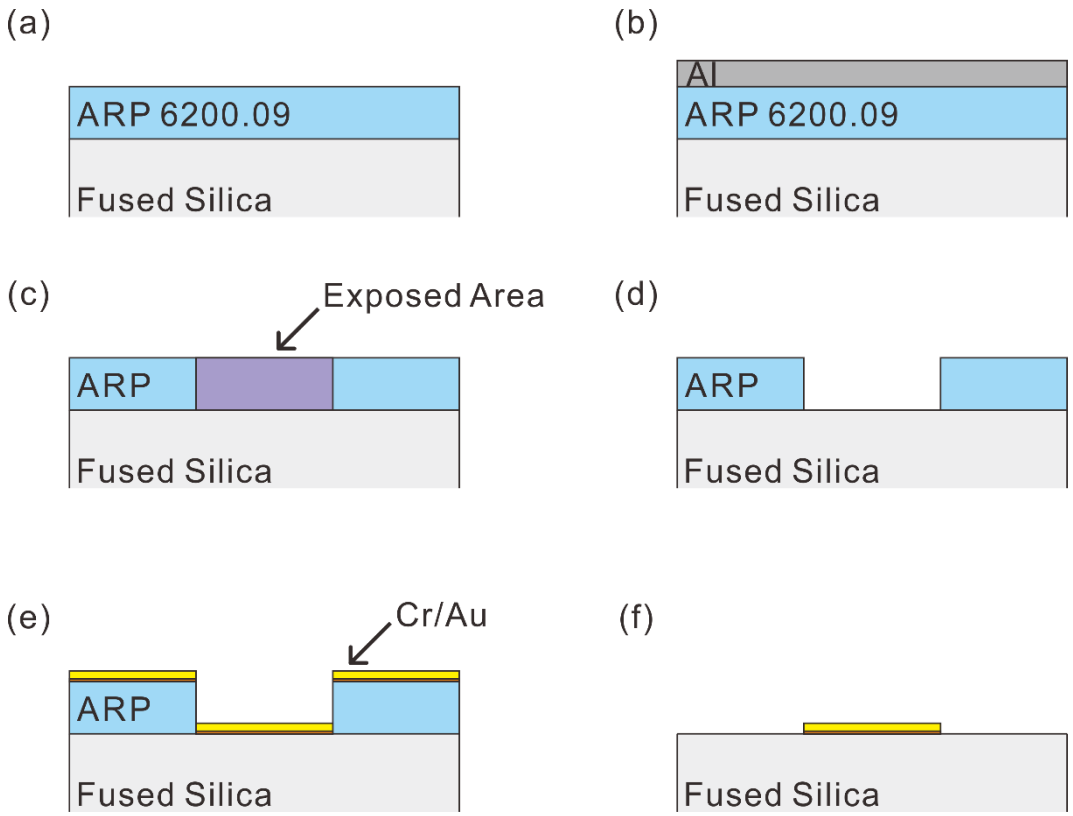

Figure 3-1. Fabrication process of the unit cell of simple metal strip array.

Figure 3-1 shows the fabrication process by using e-beam lithography. E-beam resist (ER) AR-P 6200.09 (ALL resis Inc.) is spin coated on a fused silica wafer with 4000 rpm for 60 seconds. The spin-coated sample is baked for 3 minutes at 150 ℃ on a hot plate. Then, 10-nm-thick Al is deposited on the ER to prevent charging during e-beam lithography. The pattern is written with e-beam lithography. The patterned sample is soaked in AZ MIF 300 (AZ Electronics Materials Corp.) for 60 seconds to remove Al layer. Then, the sample is developed with XAR 600_546 (All resist Inc.) for 60 seconds. For the metal strip, 2-nm-thick Cr and 18-nm-thick Au are used, since Cr increases adhesion between the SiO_2

substrate and the Au strip, and Au is stable in air. The 2-nm-thick Cr and 18-nm-thick Au is deposited by e-beam evaporator. And then, the sample lifted-off with XAR 600_71 (All resist Inc.). In this lift-off process, sample is soaked in XAR 600_71 for 24 hours, and then boiled for 30 minutes at 70 ℃ on a hot plate. If there still exists not fully lifted-off region after boiling, the samples are sonicated for a few seconds.

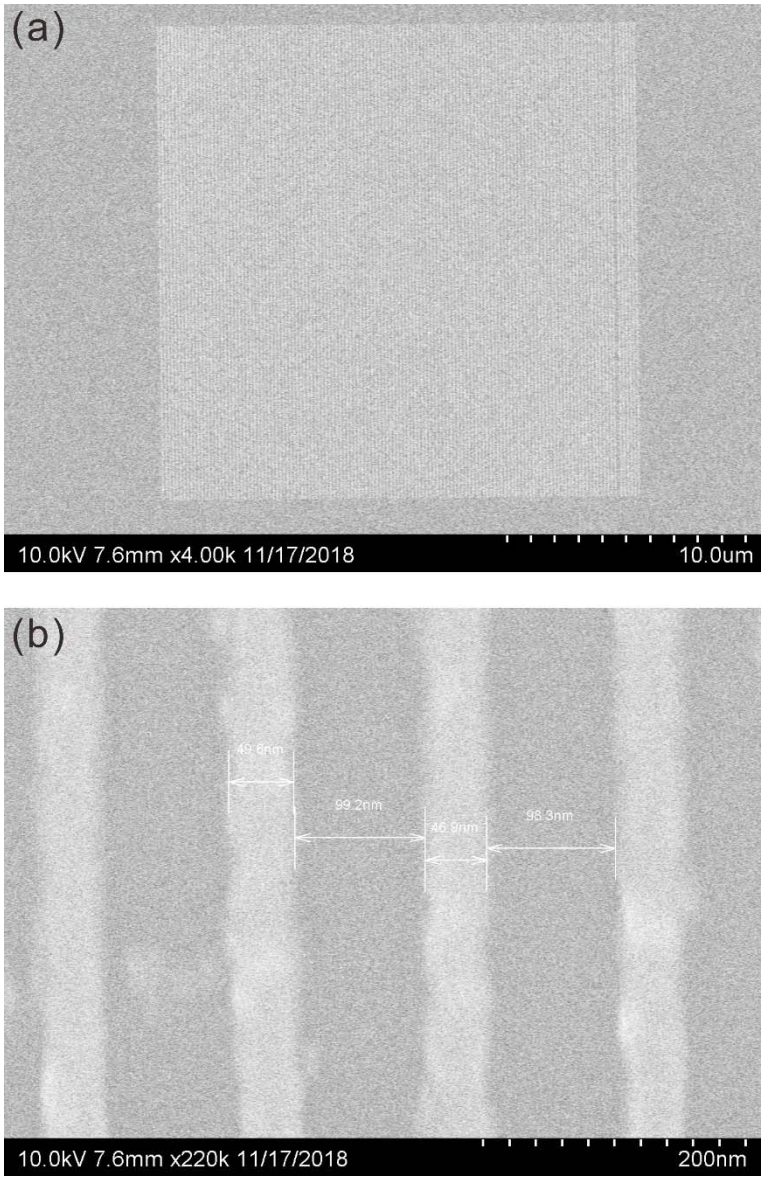

Figure 3-2. SEM image of the fabricated pattern with w = 50 nm and p = 150 nm.

Figure 3-2 shows SEM images of the fabricated pattern. The pattern size is set to 20 × 20 μm^2 for this preliminary fabrication. The metal strip consists of 2-nm-thick Cr at the bottom and 18-nm-thick Au at the top. For SEM observation, 3-nm-thick Cr is deposited on the sample with e-beam evaporator. For now, a strip width of 50 nm with a period of 150 nm strip array fabrication is possible. Since the

strip size is only tens of nanometers and the substrate is SiO_2 which has no conductivity, the Figure 3-2 (b) of magnified SEM image is looked blurred. This can be somewhat overcome with reducing charging problem with using silver paste instead of carbon tape when attaching the sample on the SEM chuck, and with depositing thicker Cr on the sample. This will be investigated in the future study.

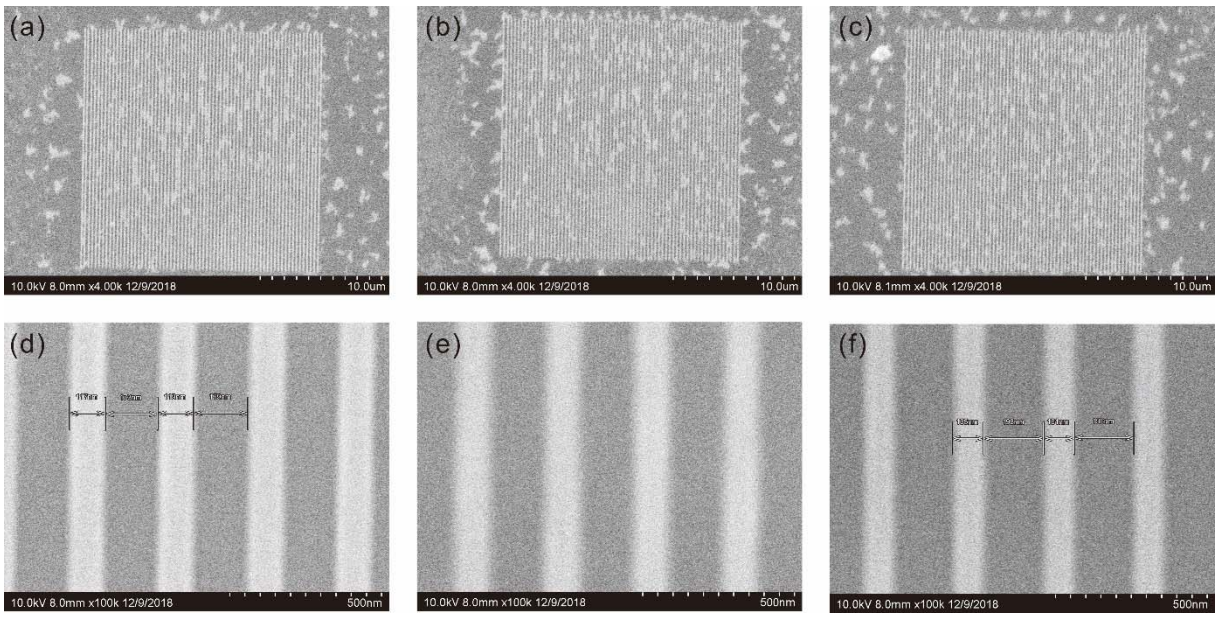

Figure 3-3. SEM image of fabricated color filters. (a), (b), and (c) are w = 100 nm with p = 300 nm, w = 90 nm with p = 300 nm, and w = 80 nm with p = 300 nm, respectively. (d), (e), and (f) are magnified image of (a), (b), and (c), respectively.

As a proof-of-concept work, subtractive color filters are fabricated as shown in Figure 3-3. The subtractive color filters have the rejection band in visible range so that the color that passed the filter can be seen. If red color is rejected, blue and green colors are seen in RGB color space. Since the LSPR around the thin metal strip causes the rejection band in transmission spectrum, the transmissive subtractive color filters can be made with thin metal strip array. Therefore, the subtractive color filters which have the rejection band at λ_r = 600 nm are fabricated for this experiment. For 2-nm-thick Cr and 18-nm-thick Au strip array, it has the rejection band at λ_r = 600 nm when w = 100 nm and p = 300 nm. To verify the rejection band shifting with the different strip width, metal strip array of w = 90 nm and w = 80 nm with the same period are also fabricated. In Figure 3-3, (a) is pattern when w = 100 nm and p = 300 nm, and (d) is a magnified image of (a). (b) is pattern when w = 90 nm and p = 300 nm, and (e) is a magnified image of (b). (c) is pattern when w = 80 nm and p = 300 nm, and (f) is a magnified image of (c). White dots on the patterns in Figure 3-3 (a), (b), and (c) are the ER residues. This will be removed in the future study.

3.2. Subtractive color filter experiment

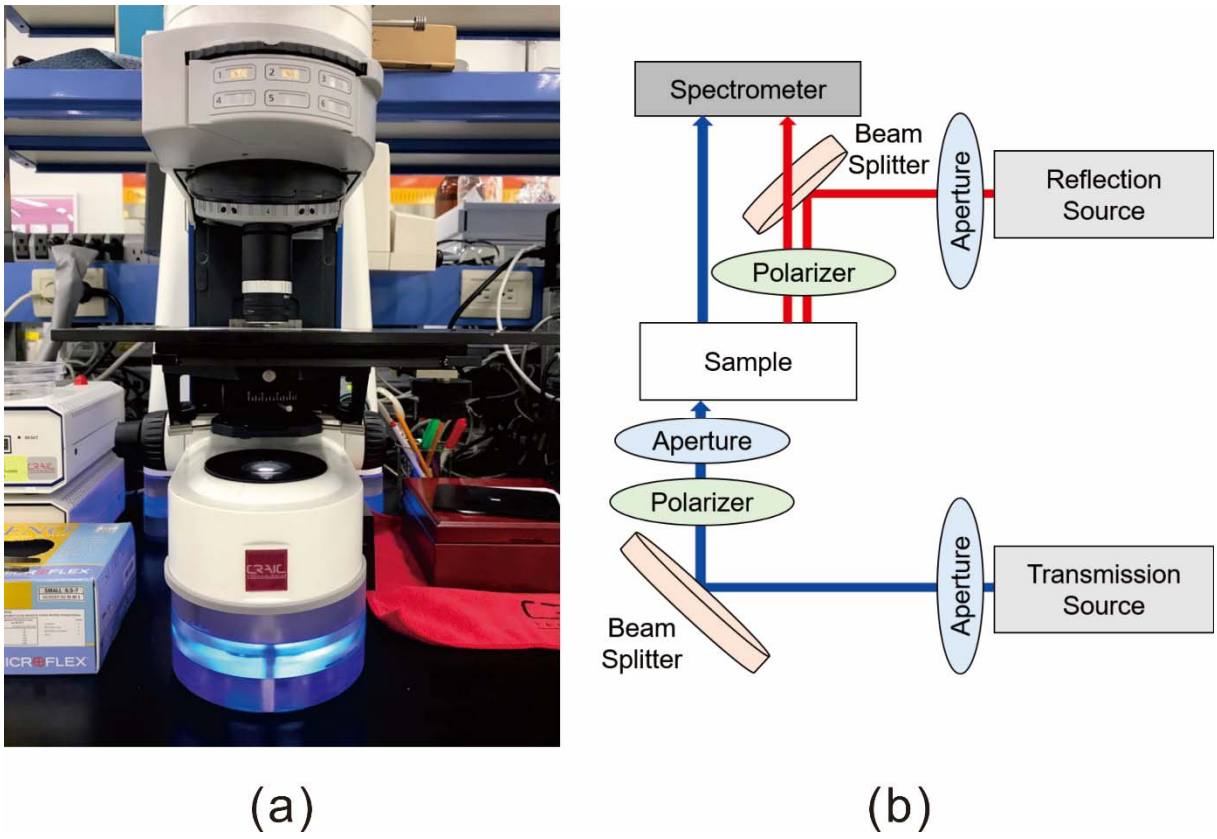

Figure 3-4. (a) The image of the UV-Vis microspectrometer and (b) schematic of experimental setup.

Figure 3-4 shows the image of the UV-Vis Microspectrometer (CRAIC Technologies) and schematic of experimental setup. Unpolarized light from the light source is polarized to p-wave. Then, the transmitted and reflected p-wave from the color filters are measured.

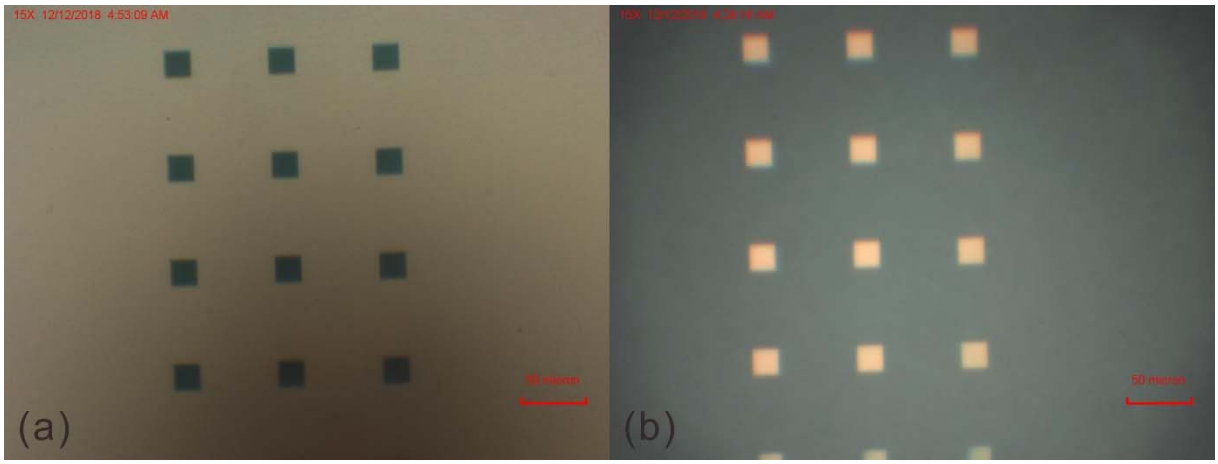

Figure 3-5. (a) The transmission image and (b) the reflection image of the patterns from the UV-Vis microspectrometer.

Figure 3-5 shows the image of transmitted and reflected p-wave from the color filters. Three columns represent w = 100 nm, w = 90 nm, and w = 80 nm from the left to the right with the p = 300 nm. For reproducibility, several doses are tested in rows. In transmission image, patterns look blue green color, since they have the rejection band at λ_r = 600 nm, corresponding to red color. On the other hand, in reflection image, patterns look light red color, since they have the resonance wavelength at λ_r = 600 nm. In addition, the region without patterns looks bright and dark in transmission and reflection image, respectively. This can be explained by their spectrum. In transmission spectrum, since the region without patterns has no rejection band, almost light can pass the filter. The region with no patterns looks bright. Whereas, in reflection spectrum, there is no reflected light in the region without patterns. Therefore, the region looks dark.

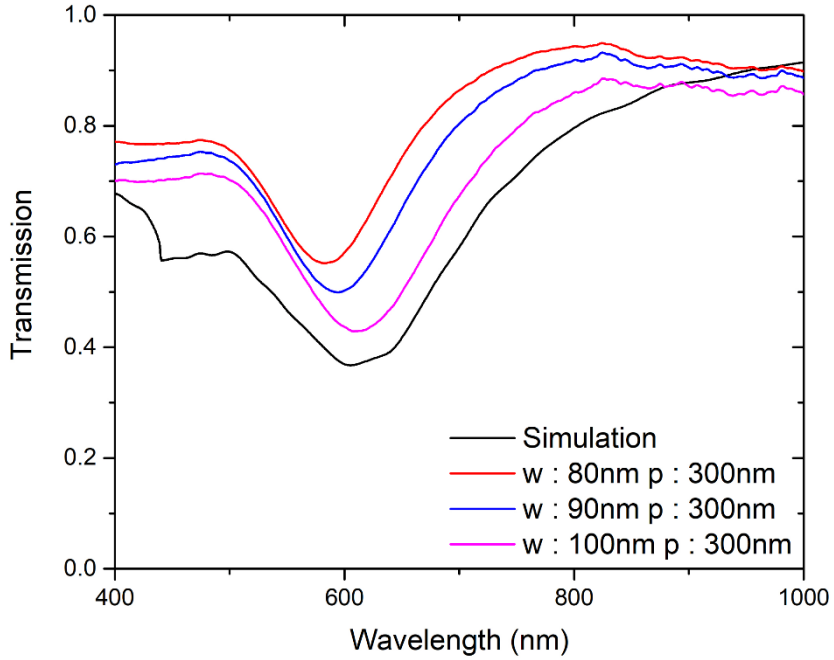

Figure 3-6. The transmission spectrum of simulation and measurement results. Black solid line indicates the result of the simulation, and red, blue, and pink solid lines indicate the measurement results of the patterns when w = 100 nm and p = 300 nm, w = 90 nm and p = 300 nm, and w = 80 nm and p = 300 nm, respectively.

Figure 3-6 shows the simulation and the experiment results of transmission spectrum. As expected in the simulation, the rejection band located around λ_r = 600 nm in the experiment. In addition, the rejection band blue-shifts as strip width w decreases as it is explained by FP relation. Outside the rejection band, lower transmission on the left-hand side than that of the right-hand side is due to the interband transition of Au. These results indicate that this preliminary experiment verifies the optical simulation results of the modulator. Reflection spectrum cannot be achieved for now due to the polarizer set up of the microspectrometer.

IV. Discussion

For the better modulation efficiency, finding the best modulation depth by adjusting the strip thickness, period and HfO_2 thickness is investigating. By increasing the strip thickness up to 20-nm-thick, the transmission can be decreased down to 1 % at λ_r = 850 nm at off-state, but the transmission increases almost 200 % at on-state, not so much different from when the strip thickness is 10 nm. In addition, when the period is reduced to $p = 2w$, the transmission can be decreased down to 2 % at λ_r = 850 nm without a bias voltage, but the increase of the transmission is similar to the case when $p = 3w$ with a bias voltage. However, the on-state voltage for $N = 1 \times 10^{22}$ cm^{-3} is increased to 54 V due to the reduce of fringing electric field by reducing the period. When reducing the HfO_2 thickness, there still exists a problem of diverging resonance dips, and the transmission at λ_r = 850 nm is increasing due to the strong interaction between the Ag strip and the Ag layer. Therefore, using two different oxides such as TiO_2 with HfO_2 or TiO_2 with Al_2O_3 to reduce the bias voltage and increase the mode confinement around the Ag strip is investigating. Because TiO_2 is high-k dielectric which permittivity is 80, and the mode can be more strongly confined around the Ag strip.

Furthermore, to compare the modulation bandwidth with direct modulation, the RC time constant should be calculated. However, since the proposed modulator is not just a parallel capacitor structure, proper models to calculate the resistivity and the capacitance are required. In addition, ITO carrier transit time also should be considered. The modulation bandwidth is determined by the dominant factor either the RC time constant or the ITO carrier transit time. Therefore, the modulation bandwidth with the consideration of both effects is investigating.

Lastly, sub-50-nm strip width of ZnO-Ag-ZnO samples are fabricating. With further experiments with these subtractive color filters, the optical characteristics of ZnO-Ag-ZnO strip array can be demonstrated. After demonstrating these simple Ag nanostrip array structures, the proposed modulator will be fabricated and experimented.

V. Conclusion

In this thesis, the near IR modulator for the indirect modulation of the IR wireless communications, consisting of ultrathin metal nanostrip array and transparent conducting oxide, is theoretically investigated. To make the resonance dip at λ_r = 850 nm, geometrical parameters of the structure are thoroughly investigated. The period p is set to 3w, to remove the coupling of the LSPR with the nearby Ag strip. The influence of the strip thickness and the strip width to the resonance wavelength are explained with Fabry-Perot resonance condition and set to t_M = 10 and w = 97, respectively. In addition, the oxide thickness t_H is set to 100 nm to remove diverged resonance dips. The electrical properties of ITO are also investigated. When a bias voltage is applied between the Ag strip and the Ag layer, the real part of the ITO refractive index decreases about 1.4 and the imaginary part of the ITO refractive index increases about 2.7 at the strip edge. This change results in the intensity modulation of the proposed modulator. The transmission increases almost 200 % at λ_r = 850 nm when off-state changes to on-state. For t_H = 10 nm, the transmission increases 5.5 % when w = 148 nm and 12 % when w = 93 nm at λ_r = 850 nm when off-state changes to on-state, but the bias voltage is 16 V.

As a preliminary experiment, 2-nm-thick Cr and 18-nm-thick Au strip array is fabricated on fused silica substrate. The fabricated w = 100 nm and p = 300 nm patterns shows good agreement between the simulation and the experiment results. In addition, the experiments of the fabricated other patterns with w = 90 nm and p = 300 nm, and w = 80 nm and p = 300 nm show red-shift as the strip width increases. This verifies the theoretical investigation of the thin metal nanostrips.

With further study of better modulation efficiency and modulation bandwidth, future realization of the proposed modulator will be possible. The proposed near IR modulator has great potential for indirect fast intensity modulator for IR wireless communications.

REFERENCES

1. S. A. Maier. *Plasmonics: Fundamentals and Applications.* New York, NY: Springer, 2007, pp. 5-34.

2. J. J. Bruke and G. I. Stegeman. “Surface-polariton-like waves guided by thin, lossy metal films.” *Physical Review B*, vol. 33, pp. 5186-5201, Apr. 1986.

3. B. Zeng, Y. Gao and F. J. Bratoli. “Ultranthin nanostructured metals for highly transmissive plasmonic subtractive color filters.” *Scientific Reports*, vol. 3, pp. 2840-2849, Oct. 2013.

4. X. L. Hu, L. B. Sun, B. Zeng, L. S. Wang, Z. G. Yu, S. A. Bai, S. M. Yang, L. X. Zhao, Q. Li, M. Qiu, R. Z. Tai, H. J. Fecht, J. Z. Jiang, and D. X. Zhang. “Polarization-independent plasmonic subtractive color filtering in ultrathin Ag nanodisks with high transmission.” *Applied Optics*, vol. 55, pp. 148-152, Jan. 2016.

5. V. R. Shrestha, S.-S. Lee, E.-S. Kim, and D.-Y. Choi. “Aluminum plasmonic based highly transmissive polarization-independent subtractive color filters exploiting a nanopatch array.” *Nano Letters*, vol. 14, pp. 6672-6678, Oct. 2014.

6. R. Yu, V. Pruneri, and F. J. G. de Abajo. “Active modulation of visible light with graphene-loaded ultrathin metal plasmonic antennas.” *Scientific Reports*, vol. 6, pp. 32144-32150, Aug. 2016.

7. X. Ni, Z. J. Wong, M. Mrejen, Y. Wang, and X. Zhang. “An ultrathin invisibility skin cloak for visible light.” *Applied Optics*, vol. 349, pp. 1310-1314, Sep. 2015.

8. D. Hu, P. Wang, Z. Zhang, L. Pang, S. Kim, and J. Du. “Anomalous reflection in the ultra-thin nano-strip antenna induced by incident field and displacement current phase matching.” *Journal of the Optical Society of America B*, vol. 32, pp. 1369-1376, Jul. 2015.

9. T. Sondergaard and S. I. Bozhevolnyi. “Metal nano-strip optical resonators.” *Optics Express*, vol. 15, pp. 4198-4204, Apr. 2007.

10. G. D. Valle, T. Sondergaard, and S. I. Bozhevolnyi. “Plasmon-polariton nano-strip resonators: from visible to infra-red.” *Optics Express*, vol. 16, 6867-6876, May. 2008.

11. T. Sondergaard, J. Beermann, A. Boltasseva, and S. I. Bozhevolnyi. “Slow-plasmon resonant-

nanostrip antennas: Analysis and demonstration." *Physical Review B*, vol. 77, pp. 115420-1-115420-5, Mar. 2008.

12. D. Reibold, F. Shao, A. Erdmann, and U. Peschel. "Extraordinary low transmission effects for ultra-thin patterned metal films" *Optics Express*, vol. 17, pp. 544-551, Jan. 2009.

13. I. S. Spevak, A. Y. Nikitin, E. V. Bezuglyi, A. Levchenko, and A. V. Kats. "Resonantly suppressed transmission and anomalously enhanced light absorption in periodically modulated ultrathin metal films" *Physical Review B*, vol. 79, pp. 161406-1-161406-4, Apr. 2009.

14. S. Xiao, J. Zhang, L. Peng, C. Jeppesen, R. Malureanu, A. Kristensen, and N. A. Mortensen. "Nearly zero transmission through periodically modulated ultrathin metal films" *Applied Physics Letters*, vol. 97, pp. 07116-1-07116-3, Aug. 2010.

15. S. Xia and N. A. Mortensen. "Surface-plasmon-polariton-induced suppressed transmission through ultrathin metal disk arrays." *Optics Letters*, vol. 36, pp. 37-39, Jan. 2011.

16. G. D'Aguanno, N. Mattiucci, A. Alu, and M. J. Bloemer. "Quenched optical transmission in ultrathin subwavelength plasmonic gratings." *Physical Review B*, vol. 83, pp. 035426-1-035426-11, Jan. 2011.

17. Q. Gan, W. Bai, S. Jiang, Y. Gao, W. Li, W. Wu, F. J. Bartoli. "Short-range surface plasmon polariton for extraordinary low transmission through ultra-thin metal films with nanopatterns." *Plasmonics*, vol. 7, pp. 47-52, Aug. 2011.

18. K. Wang, A. Nirmalathas, C. Lim, and E. Skafidas. "Experimental demonstration of a novel indoor optical wireless localization system for high-speed personal area networks." *Optics Letters*, vol. 40, pp. 1246-1249, Apr. 2015.

19. Y. Wang and H. Haas. "Dynamic load balancing with handover in hybrid Li-Fi and Wi-Fi networks." *Journal of Lightwave Technology*, vol. 33, pp. 4671-4682, Nov. 2015.

20. E. Feigenbaum, K. Diest, and H. A. Atwater. "Unity-order index change in transparent conducting oxides at visible frequencies." *Nano Letters*, vol. 10, pp. 2111-2116, May. 2010.

21. E. D. Palik. *Handbook of Optical Constants of Solids*, Orlando: Academic Press, 1985.

22. D. L. Wood, K. Nassau, T. Y. Kometani, and D. L. Nash. "Optical properties of cubic hafnia stabilized with yttria" *Applied Optics*, vol. 29, pp. 604-607, Feb. 2009.

23. Y. Lee, S.-J. Kim, J.-G. Yun, C. Kim, S.-Y. Lee, and B. Lee. “Electrically tunable multifunctional metasurface for integrating phase and amplitude modulation based on hyperbolic metamaterial substrate.” *Optics Express*, vol. 26, pp. 32063-32073, Nov. 2018.

24. A. Anopchenko, L. Tao, C. Arndt, and H. W. H. Lee. “Field-effect tunable and broadband epsilon-near-zero perfect absorbers with deep subwavelength thickness.” *ACS Photonics*, vol. 5, pp. 2631-2637, Apr. 2018.

25. F. M. Li, B. C. Bayer, S. Hofmann, S. P. Speakman, C. Ducati, W. I. Milne, and A. J. Flewitt. “High-density remote plasma sputtering of high-dielectric-constant amorphous hafnium oxide films” *Physica Status Solidi B*, vol. 250, pp. 957-967, Mar. 2013.